MOX-Report No. 54/2019

IsoGeometric Approximations for Electromagnetic Problems in Axisymmetric Domains

Simona, A.; Bonaventura, L; de Falco, C.; Schoeps, S.

MOX, Dipartimento di Matematica
Politecnico di Milano, Via Bonardi 9 - 20133 Milano (Italy)

mox-dmat@polimi.it http://mox.polimi.it

IsoGeometric Approximations for Electromagnetic Problems in Axisymmetric Domains

Abele Simona [1],[2], Luca Bonaventura[1]
Carlo de Falco [1], Sebastian Schöps [2]

December 17, 2019

(1) MOX – Modelling and Scientific Computing,
Dipartimento di Matematica, Politecnico di Milano
Via Bonardi 9, 20133 Milano, Italy
abele.simona@polimi.it, luca.bonaventura@polimi.it, carlo.defalco@gmail.com

(2) Technische Universität Darmstadt
Centre for Computational Engineering
Dolivostraße 15, 64293 Darmstadt, Germany
abele@gsc.tu-darmstadt.de, schoeps@gsc.tu-darmstadt.de

Keywords: Electromagnetic Fields, Maxwell Equations, IsoGeometric Analysis, Axisymmetric Domains, De Rham Complexes

AMS Subject Classification: 65L05, 65P10, 65Z05, 70G65, 78A35

Abstract

We propose a numerical method for the solution of electromagnetic problems on axisymmetric domains, based on a combination of a spectral Fourier approximation in the azimuthal direction with an IsoGeometric Analysis (IGA) approach in the radial and axial directions. This combination allows to blend the flexibility and accuracy of IGA approaches with the advantages of a Fourier representation on axisymmetric domains. It also allows to reduce significantly the computational cost by decoupling of the computations required for each Fourier mode. We prove that the discrete approximation spaces employed functional space constitute a closed and exact de Rham sequence. Numerical simulations of relevant benchmarks confirm the high order convergence and other computational advantages of the proposed method.

1 Introduction

The solution of the Maxwell equations on axisymmetric domains, as the one depicted in Figure 1, plays an important role in many applications, such as, for example, electrical machines, cables, the beam pipe of a particle accelerator magnet or resonating cavities. Several tailored numerical techniques to solve electromagnetic

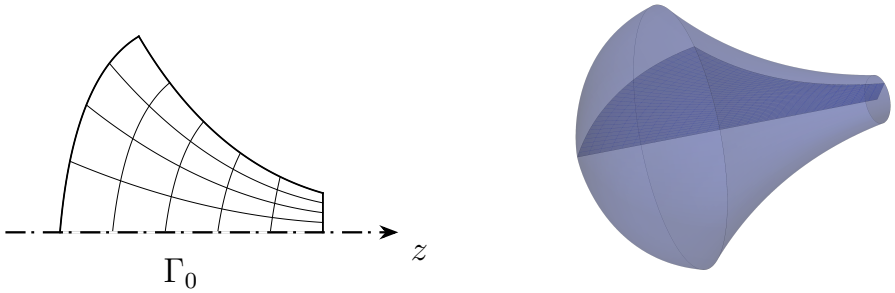

Figure 1: Representation of a cross-section S lying on the $\{\rho = 0\}$ axis (right) and its associated axisymmetric domain $\breve{\Omega}$ (right). Γ_0 represents the portion of the boundary of S on the axis.

problems on such domains have been proposed in the literature, *e.g.*, among many others, [1, 2, 3, 4, 5, 6, 7, 8, 9]. In particular, when considering the computation of multipole expansions in particle accelerator magnets, often one has to consider boundary conditions that are accurately represented by a combination of a small number of Fourier modes. Therefore, if a Fourier spectral approach is employed in the azimuthal direction, the resulting computational cost can be significantly reduced.

Concerning specifically particle accelerator simulation, it has been recently shown in [10] that the accuracy of particle tracking methods employed to design new accelerator configurations is essentially limited by the accuracy of the field reconstruction. In particular, numerical approximations of electric and magnetic fields that do not respect the inherent mathematical structure of the Maxwell equations may disrupt the effective accuracy of the simulation. This motivates the search for consistent numerical methods that provide high order accuracy in the spatial approximation.

In this work, we propose a combination of a spectral Fourier approximation in the azimuthal direction with an IsoGeometric Analysis (IGA) approach in the radial and axial directions, extending the strategy presented in [9]. The combination of the Fourier basis and IGA is in the spirit of the recent developments in [11] in computational fluid dynamics. IGA has become popular in applied electromagnetism in the last decade [12], [13]. One of its features is that it provides discrete approximations that, thanks to an appropriate choice of the finite-dimensional approximation spaces, indeed satisfy discrete analogous of the continuous Maxwell equations. In more technical terms, in the spirit of de Rham [14], sequences of functional spaces

which are closed and exact can be approximated by closed and exact sequences at a discrete level.

The combination of splines and Fourier bases in cylindrical coordinates effectively mitigates two problems. On the one hand, electrotechnical devices, particularly those based on high-frequency electromagnetic fields, are very sensitive to shape variations and are usually described by solutions of high regularity [15], which favours splines-based field and geometry representations. On the other hand, Computer Aided Design (CAD) tools rarely provide volumetric representations. Therefore, considering the cylindrical coordinate system also helps in bridging the gap between CAD and simulation. Furthermore, the orthogonality of the Fourier representation allows to decouple the computation associated to different Fourier modes. Notice that, recently, the scaled boundary approach was proposed and demonstrated for Laplace-type problems in [16]. While not limited to axisymmetric domains, this approach does not exploit the orthogonality of the Fourier basis and does not display high convergence rates of the spectral method proposed here.

The paper is structured as follows. In Section 2, we briefly recall the Maxwell equations and we introduce the notation for the treatment of problems in axisymmetric domains. Section 3 is devoted to the presentation of the strategy used to extend a general discretization in Cartesian coordinate to the cylindrical setting. Moreover, appropriate error estimates are introduced. In Section 4, we briefly introduce the discrete spaces used for IGA, together with error estimates, that will be used to build the discretization presented in Section 3. In Section 5, we apply the method presented in this work to relevant problems often arising in electromagnetism. Finally, in Section 6, we draw conclusions and discuss possible future developments of the proposed approach.

2 Preliminaries

Consider the time-harmonic Maxwell equations [17, 14]

$$\begin{aligned} \mathbf{curl}\, \boldsymbol{E} &= i\omega\, \boldsymbol{B}\ , \\ \operatorname{div} \boldsymbol{D} &= \varrho\ , \\ \mathbf{curl}\, \boldsymbol{H} &= \boldsymbol{j} - i\omega\, \boldsymbol{D}\ , \\ \operatorname{div} \boldsymbol{B} &= 0\ , \end{aligned} \tag{1}$$

together with the magnetic vector potential $\boldsymbol{A}$, for which

$$\boldsymbol{B} = \mathbf{curl}\, \boldsymbol{A}$$

holds, and a set of linear constitutive relations that links the fluxes $\boldsymbol{D}$ and $\boldsymbol{B}$ to the field strengths $\boldsymbol{E}$ and $\boldsymbol{H}$:

$$\boldsymbol{D} = \epsilon \boldsymbol{E}\ , \qquad \boldsymbol{B} = \mu \boldsymbol{H}\ ,$$

where ϵ and μ are the permittivity and permeability, respectively. A first problem, which often arises in electromagnetics and that we will consider in Sections 5.2 and 5.3, amounts to determining the eigenmodes of a resonant cavity solving the following source problem:

$$\mathbf{curl}\left(\mu^{-1}\,\mathbf{curl}\,\boldsymbol{E}\right) = \omega^2\epsilon\boldsymbol{E}\ , \tag{2}$$

with suitable boundary conditions. The second type of problem we will consider arises in the stationary limit $\omega \to 0$, and amounts to determine the magnetic vector potential $\boldsymbol{A}$ regularized by the Coulomb gauge, solving the following equations:

$$\begin{aligned} &\mathbf{curl}\left(\mu^{-1}\,\mathbf{curl}\,\boldsymbol{A}\right) = \boldsymbol{j}\ , \\ &\operatorname{div}\left(\epsilon\boldsymbol{A}\right) = 0\ , \end{aligned} \tag{3}$$

for a given source current density $\boldsymbol{j}$ and with suitable boundary conditions.

The problems above will be solved on axisymmetric bounded Lipschitz domains $\breve{\Omega} \subset \mathbb{R}^3$ represented in cylindrical coordinates. We will exploit the Fourier basis to define different de Rham complexes for each mode m, which will then be analysed and applied to some numerical examples in the following sections. In this work we will restrict our attention to the case $m \neq 0$, which corresponds to functions that are not axisymmetric. Let us introduce the cylindrical coordinates $(\rho,\, z,\, \theta)$, with the z-axis being the symmetry axis of the domain. The uncommon choice of placing the angular variable θ as the last one will considerably simplify the notation of the following considerations. The Cartesian coordinates are related to the cylindrical ones by

$$\begin{bmatrix} x \\ y \\ z \end{bmatrix} = \boldsymbol{g}\left(\begin{bmatrix} \rho \\ z \\ \theta \end{bmatrix}\right) = \begin{bmatrix} \rho\cos(\theta) \\ \rho\sin(\theta) \\ z \end{bmatrix}$$

and, conversely

$$\rho = \sqrt{x^2+y^2} \quad \text{and} \quad \theta = \begin{cases} -\arccos\left(\frac{x}{\rho}\right)\ , & \text{if } y < 0\ , \\ \arccos\left(\frac{x}{\rho}\right)\ , & \text{if } y \geq 0\ . \end{cases}$$

We describe the domain $\breve{\Omega}$ using its cross-section with respect to the and ρz-plane $S \subset \mathbb{R}^+ \times \mathbb{R}$. We assume that $S \subset \mathbb{R}^2$ is a bounded Lipschitz domain obtained through a diffeomorphism $\boldsymbol{F}$ of the unit square and that $\partial S \cap \{\rho = 0\}$ is either empty or coincides with $\boldsymbol{F}(\{0\} \times [0,\, 1])$. Let $\Gamma_0 = \operatorname{int}(\partial S \cap \{\rho = 0\})$ be the interior of the intersection of the boundary of S with the z-axis and $\Gamma = \partial S \setminus \Gamma_0$. The volume $\breve{\Omega}$ is obtained by rotating the cross-section over the symmetry axis z and adding Γ_0:

$$\breve{\Omega} = \left\{\boldsymbol{x} \in \mathbb{R}^3 : \boldsymbol{x} = \boldsymbol{g}\Big((\rho,\, z,\, \theta)^T\Big),\ (\rho,\, z)^T \in S,\ \theta \in [0,\, 2\pi)\right\} \cup \Gamma_0\ .$$

We have that $\partial\breve{\Omega} = \Gamma \times [0,\, 2\pi)$ (see Figure 1).

The differential operators involved in the standard de Rham complex in Cartesian coordinates [18]

$$\mathbb{R} \longrightarrow H^1(\breve{\Omega}) \xrightarrow{\textbf{grad}} H(\textbf{curl};\, \breve{\Omega}) \xrightarrow{\textbf{curl}} H(\mathrm{div};\, \breve{\Omega}) \xrightarrow{\mathrm{div}} L^2(\breve{\Omega}) \longrightarrow 0 \qquad (4)$$

correspond to the following ones in cylindrical coordinates:

$$\textbf{grad}^{\,\mathrm{c}}\, u = \begin{bmatrix} \partial_\rho u \\ \partial_z u \\ \dfrac{1}{\rho}\partial_\theta u \end{bmatrix} ,$$

$$\textbf{curl}^{\,\mathrm{c}}\, \boldsymbol{u} = \begin{bmatrix} \dfrac{1}{\rho}\partial_\theta u_z - \partial_z u_\theta \\ \dfrac{1}{\rho}(\partial_\rho(\rho\, u_\theta) - \partial_\theta u_\rho) \\ \partial_z u_\rho - \partial_\rho u_z \end{bmatrix} ,$$

$$\mathrm{div}^{\,\mathrm{c}}\, \boldsymbol{u} = \frac{1}{\rho}\, \partial_\rho(\rho\, u_\rho) + \frac{1}{\rho}\, \partial_\theta u_\theta + \partial_z u_z \ .$$

Since the domain is axisymmetric, we can exploit the Fourier orthogonal system in the angular variable θ. Moreover, it is convenient to express each function on $\breve{\Omega}$ as the sum of a symmetric and an antisymmetric part with respect to the plane at $\theta = 0$, so that, for a scalar function, we have that $u = u^s + u^a$, where

$$u^s = u^{(0)} + \sum_{m=1}^{\infty} u^{(m)} \cos(m\theta) \ ,$$

$$u^a = \sum_{m=1}^{\infty} u^{(-m)} \sin(m\theta) \ .$$

For a vector function we have instead that $\boldsymbol{u} = \boldsymbol{u}^s + \boldsymbol{u}^a$, where

$$\boldsymbol{u}^s = \begin{bmatrix} u_\rho^{(0)} \\ u_z^{(0)} \\ 0 \end{bmatrix} + \sum_{m=1}^{\infty} \begin{bmatrix} u_\rho^{(m)} \cos(m\theta) \\ u_z^{(m)} \cos(m\theta) \\ u_\theta^{(m)} \sin(m\theta) \end{bmatrix} ,$$

$$\boldsymbol{u}^a = \begin{bmatrix} 0 \\ 0 \\ u_\theta^{(0)} \end{bmatrix} + \sum_{m=1}^{\infty} \begin{bmatrix} u_\rho^{(-m)} \sin(m\theta) \\ u_z^{(-m)} \sin(m\theta) \\ u_\theta^{(-m)} \cos(m\theta) \end{bmatrix} .$$

The Fourier coefficients $u^{(m)}$, $\boldsymbol{u}^{(m)}$ are defined on the cross-section S. With this representation, the effect of the differential operators on each mode m can be considered independently, leading to the definition of the following operators acting on

the Fourier coefficients:

$$\mathbf{grad}^{\,\mathrm{m}}\, u^{(m)} = \begin{bmatrix} \partial_\rho u^{(m)} \\ \partial_z u^{(m)} \\ -\dfrac{m}{\rho} u^{(m)} \end{bmatrix} , \tag{5}$$

$$\mathbf{curl}^{\,\mathrm{m}}\, \boldsymbol{u}^{(m)} = \begin{bmatrix} -\dfrac{m}{\rho} u_z^{(m)} - \partial_z u_\theta^{(m)} \\ \dfrac{1}{\rho}\Big(\partial_\rho\Big(\rho\, u_\theta^{(m)}\Big) + m\, u_\rho^{(m)}\Big) \\ \partial_z u_\rho^{(m)} - \partial_\rho u_z^{(m)} \end{bmatrix} , \tag{6}$$

$$\mathrm{div}^{\,\mathrm{m}}\, \boldsymbol{u}^{(m)} = \frac{1}{\rho}\,\partial_\rho\Big(\rho\, u_\rho^{(m)}\Big) - \frac{m}{\rho} u_\theta^{(m)} + \partial_z u_z \ . \tag{7}$$

In cylindrical coordinates, the integral of a function f over a volume has the form

$$\int_{\breve{\Omega}} f\, \rho\, \mathrm{d}\rho \mathrm{d}z \mathrm{d}\theta \ .$$

This leads naturally to the use of weighted Hilbert spaces, which are defined as follows:

$$\begin{aligned} L^2_\rho(S) \qquad &= \left\{ u : \int_S u^2\, \rho\, \mathrm{d}\rho \mathrm{d}z < \infty \right\} , \\ L^2_\rho(S;\, \mathbb{R}^3) &= \left\{ \boldsymbol{u} : \int_S \|\boldsymbol{u}\|_e^2\ \rho\, \mathrm{d}\rho \mathrm{d}z < \infty \right\} , \end{aligned}$$

where $\|\boldsymbol{u}\|_e = \sqrt{\boldsymbol{u}\cdot\boldsymbol{u}}$ is the Euclidean norm and $\boldsymbol{u}$ is a vectorial function defined on S which takes values in $\mathbb{R}^3$. The associated norms are the standard ones induced by the inner products

$$(u,\, v)_{L^2_\rho(S)} = \int_S uv\, \rho\, \mathrm{d}\rho \mathrm{d}z \ , \quad (\boldsymbol{u},\, \boldsymbol{v})_{L^2_\rho(S;\,\mathbb{R}^3)} = \int_S \boldsymbol{u}\cdot\boldsymbol{v}\, \rho\, \mathrm{d}\rho \mathrm{d}z \ ,$$

and will be often simply denoted using the subscript ρ, *i.e.* $\|u\|_\rho = \sqrt{(u,\, u)_\rho}$. We also introduce the following spaces:

$$\begin{aligned} Z^{m,\,0} &= H_\rho(\mathbf{grad}^{\,\mathrm{m}};\, S) = \big\{ u \in L^2_\rho(S) : \mathbf{grad}^{\,\mathrm{m}}\, u \in L^2_\rho(S;\, \mathbb{R}^3) \big\}, \\ Z^{m,\,1} &= H_\rho(\mathbf{curl}^{\,\mathrm{m}};\, S) \ = \big\{ \boldsymbol{u} \in L^2_\rho(S;\, \mathbb{R}^3) : \mathbf{curl}^{\,\mathrm{m}}\, \boldsymbol{u} \in L^2_\rho(S;\, \mathbb{R}^3) \big\}, \\ Z^{m,\,2} &= H_\rho(\mathrm{div}^{\,\mathrm{m}};\, S) \quad = \big\{ \boldsymbol{u} \in L^2_\rho(S;\, \mathbb{R}^3) : \mathrm{div}^{\,\mathrm{m}}\, \boldsymbol{u} \in L^2_\rho(S) \big\} \ , \\ Z^{m,\,3} &= L^2_\rho(S) \ , \end{aligned} \tag{8}$$

where the differential operators have to be interpreted in a weak sense and the corresponding norms are

$$\begin{aligned} \|u\|^2_{H_\rho(\mathbf{grad}^{\,\mathrm{m}};\, S)} &= \|u\|^2_\rho + \|\mathbf{grad}^{\,\mathrm{m}}\, u\|^2_\rho \ , \\ \|\boldsymbol{u}\|^2_{H_\rho(\mathbf{curl}^{\,\mathrm{m}};\, S)} &= \|\boldsymbol{u}\|^2_\rho + \|\mathbf{curl}^{\,\mathrm{m}}\, u\|^2_\rho \ , \\ \|\boldsymbol{u}\|^2_{H_\rho(\mathrm{div}^{\,\mathrm{m}};\, S)} &= \|\boldsymbol{u}\|^2_\rho + \|\mathrm{div}^{\,\mathrm{m}}\, u\|^2_\rho \ . \end{aligned}$$

The spaces (8) arise naturally in the resolution of electromagnetic problems in cylindrical coordinates by means of Galerkin formulations. For example, for $m \neq 0$, the formulation associated to (2) with Perfect Electric Conductor (PEC) boundary conditions reads

Problem 1. *Find the eigenpair* $(\omega^2, \boldsymbol{E}^{(m)}) \in \mathbb{R}_+ \times Z_0^{m,1}$*, with* $\boldsymbol{E} \neq \boldsymbol{0}$ *and where the subscript* 0 *in the space denotes the vanishing tangential component on* Γ*, such that*

$$\int_S (\mu^{-1}\,\mathbf{curl}^m\,\boldsymbol{E}^{(m)}) \cdot \mathbf{curl}^m\,\boldsymbol{v}\,\rho\,\mathrm{d}\rho\mathrm{d}z = \omega^2 \int_S \epsilon \boldsymbol{E}^{(m)} \cdot \boldsymbol{v}\,\rho\,\mathrm{d}\rho\mathrm{d}z \quad , \quad \boldsymbol{v} \in Z_0^{m,1}\ . \tag{9}$$

The Maxwell equations (1), through the differential operators (5)–(7), relate quantities belonging to different spaces. A representation of the resulting structure is given by the sequence

$$0 \longrightarrow Z^{m,0} \xrightarrow{\mathbf{grad}^m} Z^{m,1} \xrightarrow{\mathbf{curl}^m} Z^{m,2} \xrightarrow{\mathrm{div}^m} Z^{m,3} \longrightarrow 0$$

In [9, Theorem 2.1], it has been proven that the sequence is exact for $m \neq 0$, meaning that the range of each operator linking two spaces is equal to the kernel of the subsequent one. The use of discretizations that respect the above structure is necessary to yield stable numerical methods. The aim of the following sections is to present a technique to build such discretizations, which are well-suited for the resolution of problems in electromagnetism.

3 Discretization

To solve numerical problems in electromagnetism, we need to approximate the continuous spaces $Z^{m,k}$, $k = 0, \ldots, 3$ by means of finite-dimensional subspaces $Z_h^{m,k}$ which depend on a discretization parameter related to the characteristic element size h. In the following, we will use the subscript h to refer to quantities related to the finite-dimensional spaces and we will consider conforming discretizations, meaning that $Z_h^{m,k} \subset Z^{m,k}$ for every value of h. In this section, we mimic the strategy used in [9] to build an exact sequence of conforming discrete spaces and projectors such that, for sufficiently regular functions, the following diagram commutes

$$\begin{array}{ccccccccc} 0 & \longrightarrow & Z^{m,0} & \xrightarrow{\mathbf{grad}^m} & Z^{m,1} & \xrightarrow{\mathbf{curl}^m} & Z^{m,2} & \xrightarrow{\mathrm{div}^m} & Z^{m,3} \longrightarrow 0 \\ & & \downarrow \breve{\Pi}^0 & & \downarrow \breve{\Pi}^1 & & \downarrow \breve{\Pi}^2 & & \downarrow \breve{\Pi}^3 \\ 0 & \longrightarrow & Z_h^{m,0} & \xrightarrow{\mathbf{grad}^m} & Z_h^{m,1} & \xrightarrow{\mathbf{curl}^m} & Z_h^{m,2} & \xrightarrow{\mathrm{div}^m} & Z_h^{m,3} \longrightarrow 0 \end{array} \tag{10}$$

The discrete spaces in (10) are built using sequences of two-dimensional Cartesian spaces defined on S. We therefore start introducing the standard two-dimensional

Cartesian spaces with the corresponding discrete counterparts. We first introduce the basic definitions and the necessary assumptions on the discrete spaces, postponing the explicit definition of these to the following section. Let the standard spaces of square-integrable functions in Cartesian coordinates be defined as

$$\begin{aligned} L^2(S) &= \left\{ u : \int_S u^2 \,\mathrm{d}\rho\mathrm{d}z < \infty \right\}, \\ L^2(S;\mathbb{R}^2) &= \left\{ \boldsymbol{u} : \int_S \|\boldsymbol{u}\|_e^2 \,\mathrm{d}\rho\mathrm{d}z < \infty \right\}, \end{aligned}$$

along with the associated Hilbert spaces H^s, which is the space of functions in L^2 such that the weak derivatives up to order s belong to L^2. We also define:

$$\begin{aligned} Y^0 &= H^1(S) &&= \left\{ u \in L^2(S) : \mathbf{grad}\, u \in L^2(S) \right\}, \\ Y^1 &= H(\mathrm{curl};\, S) &&= \left\{ \boldsymbol{u} \in L^2(S;\mathbb{R}^2) : \mathrm{curl}\, \boldsymbol{u} \in L^2(S) \right\}, \\ Y^{1*} &= H(\mathrm{div};\, S) &&= \left\{ \boldsymbol{u} \in L^2(S;\mathbb{R}^2) : \mathrm{div}\, \boldsymbol{u} \in L^2(S) \right\}, \\ Y^2 &= L^2(S) &&= \left\{ u : \int_S u^2 < \infty \right\}. \end{aligned} \tag{11}$$

Here, **grad** and div are the standard gradient and divergence in Cartesian coordinates

$$\mathbf{grad}\, u = \begin{bmatrix} \partial_\rho u \\ \partial_z u \end{bmatrix}, \qquad \mathrm{div}\left(\begin{bmatrix} u_\rho \\ u_z \end{bmatrix} \right) = \partial_\rho u_\rho + \partial_z u_z$$

and the scalar curl is defined as

$$\mathrm{curl}\left(\begin{bmatrix} u_\rho \\ u_z \end{bmatrix} \right) = \partial_\rho u_z - \partial_z u_\rho \,.$$

For functions in Y^0, also the following operator is well-defined:

$$\mathbf{rot}(u) = \begin{bmatrix} \partial_z u \\ -\partial_\rho u \end{bmatrix} = \mathbf{P}(\mathbf{grad}(u)) \,,$$

where

$$\mathbf{P} = \begin{bmatrix} 0 & 1 \\ -1 & 0 \end{bmatrix} .$$

We will use the word rotor, or perpendicular gradient, to indicate **rot** and to avoid the confusion with the three-dimensional **curl**. For error estimates we will also need the the spaces $H^s(\mathbf{curl};\, S)$, which is the space of functions in $H^s(S;\mathbb{R}^3)$ such that their curl belongs to $H^s(S;\mathbb{R}^3)$ and $H^s(\mathrm{div};\, S)$, which is the space of functions in $H^s(S;\mathbb{R}^3)$ such that their divergence belongs to $H^s(S)$.

We assume that Y_h^0, Y_h^1, Y_h^{1*} and Y_h^2 are conforming discretizations of (11) and that, with a sequence of L^2-stable projectors, make the following diagrams

commutative:

$$\begin{array}{ccccccccc}
\mathbb{R} & \longrightarrow & Y^0 & \xrightarrow{\mathbf{grad}} & Y^1 & \xrightarrow{\mathrm{curl}} & Y^2 & \longrightarrow & 0 \\
 & & \downarrow{\scriptstyle \Pi^0} & & \downarrow{\scriptstyle \Pi^1} & & \downarrow{\scriptstyle \Pi^2} & & \\
\mathbb{R} & \longrightarrow & Y_h^0 & \xrightarrow{\mathbf{grad}} & Y_h^1 & \xrightarrow{\mathrm{curl}} & Y_h^2 & \longrightarrow & 0
\end{array} \tag{12}$$

$$\begin{array}{ccccccccc}
\mathbb{R} & \longrightarrow & Y^0 & \xrightarrow{\mathbf{rot}} & Y^{1*} & \xrightarrow{\mathrm{div}} & Y^2 & \longrightarrow & 0 \\
 & & \downarrow{\scriptstyle \Pi^0} & & \downarrow{\scriptstyle \Pi^{1*}} & & \downarrow{\scriptstyle \Pi^2} & & \\
\mathbb{R} & \longrightarrow & Y_h^0 & \xrightarrow{\mathbf{rot}} & Y_h^{1*} & \xrightarrow{\mathrm{div}} & Y_h^2 & \longrightarrow & 0
\end{array} \tag{13}$$

Both the continuous and the discrete sequences in (12) and (13) are exact for simply connected domains [18, 19]. Moreover we assume that the following estimates hold:

$$\begin{aligned}
\left\|u - \Pi^0 u\right\|_{H^1(S)} &\leq C h^s \left\|u\right\|_{H^{s+1}(S)} , \quad && u \in H^{s+1}(S) , \\
\left\|\boldsymbol{u} - \Pi^1 \boldsymbol{u}\right\|_{H(\mathrm{curl};\, S)} &\leq C h^s \left\|\boldsymbol{u}\right\|_{H^s(\mathrm{curl};\, S)} , \quad && \boldsymbol{u} \in H^s(\mathrm{curl};\, S) , \\
\left\|\boldsymbol{u} - \Pi^{1*} \boldsymbol{u}\right\|_{H(\mathrm{div};\, S)} &\leq C h^s \left\|\boldsymbol{u}\right\|_{H^s(\mathrm{div};\, S)} , \quad && \boldsymbol{u} \in H^s(\mathrm{div};\, S) , \\
\left\|u - \Pi^2 u\right\|_{L^2(S)} &\leq C h^s \left\|u\right\|_{H^s(S)} , && u \in H^s(S).
\end{aligned} \tag{14}$$

In [9], the discrete Cartesian spaces were chosen as piecewise linear for Y_h^0, lowest order Nedelec for Y_h^1, lowest order Raviart-Thomas for Y_h^{1*} and piecewise constant for Y_h^2. In this work, we will use IGA spaces that will be introduced in the next section.

The strategy to define the discrete counterparts of (8) is based on the use of operators that link the spaces in cylindrical coordinates to the standard spaces in Cartesian coordinates. The definition of the discrete spaces and of the projectors, together with error estimates, are then deduced from those defined for the spaces in Cartesian coordinates. The diagram

$$\begin{array}{ccccccc}
Z^{m,0} & \xrightarrow{\mathbf{grad}^m} & Z^{m,1} & \xrightarrow{\mathbf{curl}^m} & Z^{m,2} & \xrightarrow{\mathrm{div}^m} & Z^{m,3} \\
\downarrow{\scriptstyle \eta_{m,0}} & & \downarrow{\scriptstyle \eta_{m,1}} & & \downarrow{\scriptstyle \eta_{m,2}} & & \downarrow{\scriptstyle \eta_{m,3}} \\
Y^0 & \xrightarrow{\boldsymbol{G}} & Y^1 \times Y^0 & \xrightarrow{\boldsymbol{C}} & Y^{1*} \times Y^2 & \xrightarrow{D} & Y^2 \\
\downarrow{\scriptstyle \Pi^0} & & \downarrow{\scriptstyle \Pi^1 \times \Pi^0} & & \downarrow{\scriptstyle \Pi^{1*} \times \Pi^2} & & \downarrow{\scriptstyle \Pi^2} \\
Y_h^0 & \xrightarrow{\boldsymbol{G}} & Y_h^1 \times Y_h^0 & \xrightarrow{\boldsymbol{C}} & Y_h^{1*} \times Y_h^2 & \xrightarrow{D} & Y_h^2 \\
\downarrow{\scriptstyle \eta_{m,0}^{-1}} & & \downarrow{\scriptstyle \eta_{m,1}^{-1}} & & \downarrow{\scriptstyle \eta_{m,2}^{-1}} & & \downarrow{\scriptstyle \eta_{m,3}^{-1}} \\
Z_h^{m,0} & \xrightarrow{\mathbf{grad}^m} & Z_h^{m,1} & \xrightarrow{\mathbf{curl}^m} & Z_h^{m,2} & \xrightarrow{\mathrm{div}^m} & Z_h^{m,3}
\end{array} \tag{15}$$

summarizes the general strategy for the discretization that will be explained in the remaining section.

The first step is the definition of a set of operators $\eta_{m,\,k},\ k = 0,\ 1,\ 2,\ 3$ that maps functions from $Z^{m,\,k}$ onto the functional spaces defined in Cartesian coordinates

$$
\begin{aligned}
&\eta_{m,\,0} : Z^{m,\,0} \to Y^0, && u \mapsto \frac{m}{\rho} u, \\
&\eta_{m,\,1} : Z^{m,\,1} \to Y^1 \times Y^0, && \boldsymbol{u} \mapsto \begin{bmatrix} \dfrac{1}{\rho}(m\, u_\rho + u_\theta) \\ \dfrac{m}{\rho} u_z \\ u_\theta \end{bmatrix}, \\
&\eta_{m,\,2} : Z^{m,\,2} \to Y^{1*} \times Y^2, && \boldsymbol{u} \mapsto \begin{bmatrix} u_\rho \\ u_z \\ \dfrac{1}{\rho}(m u_\theta - u_\rho) \end{bmatrix}, \\
&\eta_{m,\,3} : Z^{m,\,3} \to Y^2, && u \mapsto u\ .
\end{aligned}
$$

These operators are chosen such that $\boldsymbol{G}$, $\boldsymbol{C}$ and D are both well-defined and make the top part of the diagram (15) commutative. Note that, if $\Gamma^0 \neq \emptyset$, these operators are well-defined only on regular subspaces $\widetilde{Z}^{m,\,k} \subset Z^{m,\,k}$ where

$$
\begin{aligned}
\widetilde{Z}^{m,\,0} &= \left\{ u \in Z^{m,\,0} :\ \eta_{m,\,0}(u) \in Y^0 \right\}, \\
\widetilde{Z}^{m,\,1} &= \left\{ \boldsymbol{u} \in Z^{m,\,1} :\ \eta_{m,\,1}(\boldsymbol{u}) \in Y^1 \times Y^0 \right\}, \\
\widetilde{Z}^{m,\,2} &= \left\{ \boldsymbol{u} \in Z^{m,\,2} :\ \eta_{m,\,2}(\boldsymbol{u}) \in Y^{1*} \times Y^2 \right\}, \\
\widetilde{Z}^{m,\,3} &= \left\{ u \in Z^{m,\,3} :\ \eta_{m,\,3}(u) \in Y^2 \right\}.
\end{aligned}
$$

Then, since proper conforming discretizations are known for the spaces in Cartesian coordinates (12)–(13), the discrete spaces $Z_h^{m,\,k}$ are built from the Cartesian discrete spaces using $\eta_{m,\,k}^{-1}$, *i.e.*

$$
\begin{aligned}
Z_h^{m,\,0} &= \left\{ u_h \mid u_h = \eta_{m,\,0}^{-1}(\widetilde{u}_h),\ \widetilde{u}_h \in Y_h^0 \right\}, \\
Z_h^{m,\,1} &= \left\{ \boldsymbol{u}_h \mid \boldsymbol{u}_h = \eta_{m,\,1}^{-1}(\widetilde{\boldsymbol{u}}_h),\ \widetilde{\boldsymbol{u}}_h \in Y_h^1 \times Y_h^0 \right\}, \\
Z_h^{m,\,2} &= \left\{ \boldsymbol{u}_h \mid \boldsymbol{u}_h = \eta_{m,\,2}^{-1}(\widetilde{\boldsymbol{u}}_h),\ \widetilde{\boldsymbol{u}}_h \in Y_h^{1*} \times Y_h^2 \right\}, \\
Z_h^{m,\,3} &= \left\{ u_h \mid u_h = \eta_{m,\,3}^{-1}(\widetilde{u}_h),\ \widetilde{u}_h \in Y_h^2 \right\}.
\end{aligned}
\tag{16}
$$

Consistently with this definition, we denote functions defined on spaces in Cartesian coordinates with a tilde. Moreover, since in the following discussion the ρ and z components will be often treated differently from the θ component, we will denote with the subscript ρz the meridian component of a function $\boldsymbol{u}_{\rho z} = (u_\rho,\, u_z)^T$. In order to apply the differential operators to the discrete functions, it is useful to

define, by composition, the following operators that act directly on the continuous spaces defined in Cartesian coordinates:

$$\begin{aligned} \mathbf{grad}_\star^m &= \eta_{m,0}^{-1} \circ \mathbf{grad}^m : Y^0 \to Z^{m,1} \ , \\ \mathbf{grad}_\star^m\,(\widetilde{u}) &= \begin{bmatrix} \dfrac{1}{m}(\widetilde{u} + \rho\,\partial_\rho \widetilde{u}) \\ \dfrac{\rho}{m}\partial_z \widetilde{u} \\ -\widetilde{u} \end{bmatrix} \ , \end{aligned} \tag{17}$$

$$\begin{aligned} \mathbf{curl}_\star^m &= \eta_{m,1}^{-1} \circ \mathbf{curl}^m : Y^1 \times Y^0 \to Z^{m,2} \ , \\ \mathbf{curl}_\star^m\,(\widetilde{\boldsymbol{u}}) &= \begin{bmatrix} -\widetilde{u}_z - \partial_z \widetilde{u}_\theta \\ \widetilde{u}_\rho + \partial_\rho \widetilde{u}_\theta \\ \dfrac{1}{m}(\partial_z(\rho\,\widetilde{u}_\rho) - \partial_\rho(\rho\,\widetilde{u}_z) - \partial_z \widetilde{u}_\theta) \end{bmatrix} , \end{aligned} \tag{18}$$

$$\begin{aligned} \mathrm{div}_\star^m &= \eta_{m,2}^{-1} \circ \mathrm{div}^m : Y^{1*} \times Y^2 \to Z^{m,3} \ , \\ \mathrm{div}_\star^m\,(\widetilde{\boldsymbol{u}}) &= \partial_\rho \widetilde{u}_\rho - \widetilde{u}_\theta + \partial_z \widetilde{u}_z \ . \end{aligned} \tag{19}$$

Note that, due to the choice of the spaces in Cartesian coordinates, all the differential operators (17)–(19) are well-defined. Moreover, since the discrete spaces in Cartesian coordinates are conforming, we have the following result:

Lemma 1. *The discrete spaces* (16) *are conforming in the spaces defined in* (8)*.*

Proof. We have to show that $Z_h^{m,k} \subset Z^{m,k}$, $k = 1, \ldots, 3$. Due to the boundness of S, there exists $R > 0$ such that $0 < \rho < R$, $(\rho,\, z) \in S$. Considering $\widetilde{u}_h \in Y_h^0$, we have that $\widetilde{u}_h \in Y^0$ because of the conforming discretization of the Cartesian complexes (12)–(13). So $u_h \in Z^{m,0}$, in fact

$$\|u_h\|_\rho^2 = \|\rho \widetilde{u}_h\|_\rho^2 \leq R^3 \ \|\widetilde{u}_h\|^2 < \infty$$

and

$$\begin{aligned} \|\mathbf{grad}^m\, u_h\|_\rho^2 = \|\mathbf{grad}_\star^m\, \widetilde{u}_h\|_\rho^2 &\leq R\ \|\mathbf{grad}_\star^m\, \widetilde{u}_h\|^2 \\ &\leq 3R\ \|\widetilde{u}_h\|^2 + 2R^3\ \|\mathbf{grad}\, \widetilde{u}_h\|^2 < \infty \end{aligned}$$

since $\widetilde{u}_h \in Y^0$. The proofs of the other cases are similar. For $Z_h^{m,1} \subset Z^{m,1}$, given $\boldsymbol{u}_h \in Z_h^{m,1}$, we have that

$$\begin{aligned} \|\boldsymbol{u}_h\|_\rho^2 &= \left\| \frac{1}{m}(\rho\, \widetilde{u}_{\rho,h} - \widetilde{u}_{\theta,h}) \right\|_\rho^2 + \left\| \frac{\rho}{m} \widetilde{u}_{z,h} \right\|_\rho^2 + \|\widetilde{u}_{\theta,h}\|_\rho^2 \\ &\leq 2R^3\ \|\widetilde{u}_{\rho,h}\|^2 + R^3\ \|\widetilde{u}_{z,h}\|^2 + 3R\ \|\widetilde{u}_{\theta,h}\|^2 < \infty \end{aligned}$$

and

$$\begin{aligned}\|\mathbf{curl}^m\, \boldsymbol{u}_h\|_\rho^2 &= \|\mathbf{curl}_\star^m\, \widetilde{\boldsymbol{u}}_h\|_\rho^2 \\ &= \|\widetilde{\boldsymbol{u}}_{\rho z,\,h} + \mathbf{grad}\, \widetilde{u}_{\theta,\,h}\|_\rho^2 \\ &+ \left\| \frac{1}{m}(-\rho\ \mathrm{curl}\, \widetilde{\boldsymbol{u}}_{\rho z,\,h} - \widetilde{u}_{z,\,h} - \partial_z \widetilde{u}_{\theta,\,h}) \right\|_\rho^2 \\ &\leq 6\ \|\widetilde{\boldsymbol{u}}_{\rho z,\,h}\|_\rho^2 + 4\ \|\rho\ \mathrm{curl}\, \widetilde{\boldsymbol{u}}_{\rho z,\,h}\|_\rho^2 + 4\ \|\mathbf{grad}\, \widetilde{u}_{\theta,\,h}\|_\rho^2 \\ &\leq 6R\ \|\widetilde{\boldsymbol{u}}_{\rho z,\,h}\|^2 + 4R^3\ \|\mathrm{curl}\, \widetilde{\boldsymbol{u}}_{\rho z,\,h}\|^2 + 4R\ \|\mathbf{grad}\, \widetilde{u}_{\theta,\,h}\|^2 < \infty\end{aligned}$$

since $\widetilde{\boldsymbol{u}}_{\rho z,\,h} \in Y^1$ and $\widetilde{u}_{\theta,\,h} \in Y^0$.
For $Z_h^{m,\,2} \subset Z^{m,\,2}$, given $\boldsymbol{u}_h \in Z_h^{m,\,2}$, we have that

$$\begin{aligned}\|\boldsymbol{u}_h\|_\rho^2 &= \|\widetilde{\boldsymbol{u}}_{\rho z,\,h}\|_\rho^2 + \left\| \frac{1}{m}(\rho\, \widetilde{u}_{\theta,\,h} + \widetilde{u}_{\rho,\,h}) \right\|_\rho^2 \\ &\leq 3R\ \|\widetilde{\boldsymbol{u}}_{\rho z,\,h}\|^2 + 2R^3\ \|\widetilde{u}_{\theta,\,h}\|^2 < \infty\end{aligned}$$

and

$$\begin{aligned}\|\mathrm{div}^m\, \boldsymbol{u}_h\|_\rho^2 = \|\mathrm{div}_\star^m\, \widetilde{\boldsymbol{u}}_h\|_\rho^2 &\leq 2\ \|\mathrm{div}\, \widetilde{\boldsymbol{u}}_{\rho z,\,h}\|_\rho^2 + 2\ \|\widetilde{u}_{\theta,\,h}\|_\rho^2 \\ &\leq 2R\ \|\mathrm{div}\, \widetilde{\boldsymbol{u}}_{\rho z,\,h}\|^2 + 2R\ \|\widetilde{u}_{\theta,\,h}\|^2 < \infty\end{aligned}$$

since $\widetilde{\boldsymbol{u}}_{\rho z,\,h} \in Y^{1*}$ and $\widetilde{u}_{\theta,\,h} \in Y^2$.
Finally, $Z_h^{m,\,3} \subset Z^{m,\,3}$, given $u_h \in Z_h^{m,\,3}$, we have that

$$\|u_h\|_\rho^2 = \|\widetilde{u}_h\|_\rho^2 \leq R\ \|\widetilde{u}_h\|^2 < \infty$$

since $\widetilde{u}_h \in Y^2$. □

The projectors $\breve{\Pi}^{m,\,k} : \widetilde{Z}^{m,\,k} \to Z_h^{m,\,k}$ are defined as in [9], exploiting those used in Cartesian coordinates (12)–(13), that is

$$\begin{aligned}\breve{\Pi}^0 u &= \Big(\eta_{m,\,0}^{-1} \circ \Pi^0 \circ \eta_{m,\,0}\Big)(u)\ , && u \in \widetilde{Z}^{m,\,0}\ , \\ \breve{\Pi}^1 \boldsymbol{u} &= \Big(\eta_{m,\,1}^{-1} \circ \big(\Pi^1 \times \Pi^0\big) \circ \eta_{m,\,1}\Big)(\boldsymbol{u})\ , && \boldsymbol{u} \in \widetilde{Z}^{m,\,1}\ , \\ \breve{\Pi}^2 \boldsymbol{u} &= \Big(\eta_{m,\,2}^{-1} \circ \big(\Pi^{1*} \times \Pi^2\big) \circ \eta_{m,\,2}\Big)(\boldsymbol{u})\ , && \boldsymbol{u} \in \widetilde{Z}^{m,\,2}\ , \\ \breve{\Pi}^3 u &= \Big(\eta_{m,\,3}^{-1} \circ \Pi^2 \circ \eta_{m,\,3}\Big)(u) = \Pi^2(u)\ , && u \in \widetilde{Z}^{m,\,3}\ .\end{aligned} \tag{20}$$

The following lemma shows that they are actually projectors.

Lemma 2. *The interpolators* (20) *are projectors, that is*

$$\breve{\Pi}^0 u_h = u_h\ , \qquad u_h \in Z_h^0\ , \tag{21}$$

$$\breve{\Pi}^1 \boldsymbol{u}_h = \boldsymbol{u}_h\ , \qquad \boldsymbol{u}_h \in Z_h^1\ , \tag{22}$$

$$\breve{\Pi}^2 \boldsymbol{u}_h = \boldsymbol{u}_h\ , \qquad \boldsymbol{u}_h \in Z_h^2\ , \tag{23}$$

$$\breve{\Pi}^3 u_h = u_h\ , \qquad u_h \in Z_h^3\ . \tag{24}$$

Proof. For (24) the result is immediate since the projector coincides with the one defined on the Cartesian space. Also for (21)–(23) the result is trivial and due to the definition of the spaces and to the result in Cartesian coordinates. Taking, for example (21), $u_h \in Z_h^0$, we have that

$$\breve{\Pi}^0 u_h = \Pi^0(\eta_{m,0}(u_h)) = \Pi^0(\widetilde{u}_h) = \widetilde{u}_h \ , \qquad \widetilde{u}_h \in Y_h^0 \ .$$

□

We show that the continuous and discrete spaces, together with the projectors, form a commutative diagram. We start proving the commutativity of the top part of the diagram (15).

Lemma 3. *The following diagram commutes:*

$$\begin{array}{ccccccc}
\widetilde{Z}^{m,0} & \xrightarrow{\mathbf{grad}^m} & \widetilde{Z}^{m,1} & \xrightarrow{\mathbf{curl}^m} & \widetilde{Z}^{m,2} & \xrightarrow{\mathrm{div}^m} & \widetilde{Z}^{m,3} \\
\downarrow{\scriptstyle \eta_{m,0}} & & \downarrow{\scriptstyle \eta_{m,1}} & & \downarrow{\scriptstyle \eta_{m,2}} & & \downarrow{\scriptstyle \eta_{m,3}} \\
Y^0 & \xrightarrow{\boldsymbol{G}} & Y^1 \times Y^0 & \xrightarrow{\boldsymbol{C}} & Y^{1*} \times Y^2 & \xrightarrow{D} & Y^2
\end{array}$$

Proof. For the first part involving the gradient, we have that

$$(\boldsymbol{\eta}_{1,m} \circ \mathbf{grad}^m)u = (\mathbf{G} \circ \eta_{0,m})u \ , \qquad u \in \widetilde{Z}^{m,0} \ .$$

In fact, in the left-hand side we have that

$$\begin{aligned}
\mathbf{grad}^m u &= \left(\partial_\rho u,\, \partial_z u,\, -\frac{m}{\rho}u\right)^T \ , \\
\boldsymbol{\eta}_{1,m} \circ \mathbf{grad}^m u &= \left(\frac{1}{\rho}\left(m\,\partial_\rho u - \frac{m}{\rho}u\right),\, \frac{m}{\rho}\partial_z u,\, -\frac{m}{\rho}u\right) \\
&= \left(\partial_\rho\left(\frac{m}{\rho}u\right),\, \partial_z\left(\frac{m}{\rho}u\right),\, -\frac{m}{\rho}u\right),
\end{aligned}$$

which is clearly equal to the right-hand side, since $\eta_{0,m}u = \frac{m}{\rho}u \in Y^0$, and belongs to $Y^1 \times Y^0$.
For the part involving the curl $(\boldsymbol{\eta}_{2,m} \circ \mathbf{curl}^m)\boldsymbol{u} = (\mathbf{C} \circ \boldsymbol{\eta}_{1,m})\boldsymbol{u}$, $\boldsymbol{u} \in \widetilde{\boldsymbol{Z}}^{m,1}$. In fact,

in the left-hand side we have that

$$\mathbf{curl}^m \boldsymbol{u} = \begin{bmatrix} -\dfrac{m}{\rho} u_z - \partial_z u_\theta \\ \dfrac{1}{\rho}(\partial_\rho(\rho\, u_\theta) + m\, u_\rho) \\ \partial_z u_\rho - \partial_\rho u_z \end{bmatrix},$$

$$\boldsymbol{\eta}_{2,\,m} \circ \mathbf{curl}^m \boldsymbol{u} = \begin{bmatrix} -\dfrac{m}{\rho} u_z - \partial_z u_\theta \\ \dfrac{1}{\rho}(u_\theta + m\, u_\rho) + \partial_\rho u_\theta \\ \dfrac{1}{\rho}\left(m\partial_z u_\rho - m\partial_\rho u_z + \dfrac{m}{\rho} u_z + \partial_z u_\theta \right) \end{bmatrix}$$

$$= \begin{bmatrix} -\dfrac{m}{\rho} u_z - \partial_z u_\theta \\ \dfrac{1}{\rho}(u_\theta + m\, u_\rho) + \partial_\rho u_\theta \\ -\partial_\rho\left(\dfrac{m}{\rho} u_z \right) + \partial_z\left(\dfrac{1}{\rho}(m\, u_\rho + u_\theta) \right) \end{bmatrix},$$

which is equal to the right-hand side $\mathbf{C} \circ \boldsymbol{\eta}_{1,\,m}\boldsymbol{u}$ which belongs to $Y^{1*} \times Y^2$. Finally, for the divergence part, we have that $(\eta_{3,\,m} \circ \mathrm{div}^m)\boldsymbol{u} = (D \circ \boldsymbol{\eta}_{2,\,m})\boldsymbol{u}$, $\boldsymbol{u} \in \widetilde{\boldsymbol{Z}}^{m,\,2}$. In fact, in the left-hand side we have that

$$\eta_{3,\,m} \circ \mathrm{div}^m \boldsymbol{u} = \mathrm{div}^m \boldsymbol{u} = \partial_\rho u_\rho + \partial_z u_z - \frac{1}{\rho}(m\, u_\theta - u_\rho)$$

which belongs to Y^2 and is clearly equal to the right-hand side, since

$$\boldsymbol{\eta}_{2,\,m}\boldsymbol{u} = \left(u_\rho,\, u_z,\, \frac{1}{\rho}(m\, u_\theta - u_\rho) \right)^T .$$

□

We have an analogous result for also for the bottom part of the diagram (15):

Lemma 4. *The following diagram commutes:*

$$\begin{array}{ccccccc} Y_h^0 & \xrightarrow{\boldsymbol{G}} & Y_h^1 \times Y_h^0 & \xrightarrow{\boldsymbol{C}} & Y_h^{1*} \times Y_h^2 & \xrightarrow{D} & Y_h^2 \\ \downarrow{\scriptstyle \eta_{m,\,0}^{-1}} & & \downarrow{\scriptstyle \eta_{m,\,1}^{-1}} & & \downarrow{\scriptstyle \eta_{m,\,2}^{-1}} & & \downarrow{\scriptstyle \eta_{m,\,3}^{-1}} \\ Z_h^{m,\,0} & \xrightarrow{\mathbf{grad}^m} & Z_h^{m,\,1} & \xrightarrow{\mathbf{curl}^m} & Z_h^{m,\,2} & \xrightarrow{\mathrm{div}^m} & Z_h^{m,\,3} \end{array} \tag{25}$$

Proof. The proof is analogous to the one of Lemma 3. □

The next step is to prove that the middle part of the diagram (15), formed by the spaces in Cartesian coordinates and the corresponding projectors, commutes.

Lemma 5. *The following diagram commutes:*

$$\begin{array}{ccccccc}
Y^0 & \xrightarrow{\boldsymbol{G}} & Y^1 \times Y^0 & \xrightarrow{\boldsymbol{C}} & Y^{1*} \times Y^2 & \xrightarrow{D} & Y^2 \\
\downarrow{\scriptstyle \Pi^0} & & \downarrow{\scriptstyle \Pi^1 \times \Pi^0} & & \downarrow{\scriptstyle \Pi^{1*} \times \Pi^2} & & \downarrow{\scriptstyle \Pi^2} \\
Y_h^0 & \xrightarrow{\boldsymbol{G}} & Y_h^1 \times Y_h^0 & \xrightarrow{\boldsymbol{C}} & Y_h^{1*} \times Y_h^2 & \xrightarrow{D} & Y_h^2
\end{array}$$

Proof. For the gradient and divergence part the result is an immediate consequence of the commutativity of the standard two-dimensional diagrams in Cartesian coordinates (12) and (13). For the curl part, we need to show that $\mathbf{C} \circ \left(\boldsymbol{\Pi}^1 \times \Pi^0\right) = \left(\boldsymbol{\Pi}^{1*} \times \Pi^2\right) \circ \mathbf{C}$. For the rotor and the curl the result is immediate:

$$\begin{aligned}
\mathbf{rot}\left(\Pi^0 \widetilde{u}_\theta\right) &= \boldsymbol{\Pi}^{1*}(\mathbf{rot}\, \widetilde{u}_\theta) \ , \\
\operatorname{curl}\left(\boldsymbol{\Pi}^1 \widetilde{\boldsymbol{u}}_{\rho z}\right) &= \Pi^2(\operatorname{curl} \widetilde{\boldsymbol{u}}_{\rho z}) \ .
\end{aligned}$$

Concerning the other components we have that

$$\mathbf{P}\boldsymbol{\Pi}^1(\widetilde{\boldsymbol{u}}_{\rho z}) = \boldsymbol{\Pi}^{1*}(\mathbf{P}\widetilde{\boldsymbol{u}}_{\rho z})$$

since $Y^{1*} = \mathbf{P}Y^1$ and $Y_h^{1*} = \mathbf{P}Y_h^1$. □

Finally, Lemmas 3–5 lead to the following result:

Lemma 6. *The following diagram commutes:*

$$\begin{array}{ccccccc}
\widetilde{Z}^{m,0} & \xrightarrow{\mathbf{grad}^m} & \widetilde{Z}^{m,1} & \xrightarrow{\mathbf{curl}^m} & \widetilde{Z}^{m,2} & \xrightarrow{\mathrm{div}^m} & \widetilde{Z}^{m,3} \\
\downarrow{\scriptstyle \eta_{m,0}} & & \downarrow{\scriptstyle \eta_{m,1}} & & \downarrow{\scriptstyle \eta_{m,2}} & & \downarrow{\scriptstyle \eta_{m,3}} \\
Y^0 & \xrightarrow{\boldsymbol{G}} & Y^1 \times Y^0 & \xrightarrow{\boldsymbol{C}} & Y^{1*} \times Y^2 & \xrightarrow{D} & Y^2 \\
\downarrow{\scriptstyle \Pi^0} & & \downarrow{\scriptstyle \Pi^1 \times \Pi^0} & & \downarrow{\scriptstyle \Pi^{1*} \times \Pi^2} & & \downarrow{\scriptstyle \Pi^2} \\
Y_h^0 & \xrightarrow{\boldsymbol{G}} & Y_h^1 \times Y_h^0 & \xrightarrow{\boldsymbol{C}} & Y_h^{1*} \times Y_h^2 & \xrightarrow{D} & Y_h^2 \\
\downarrow{\scriptstyle \eta_{m,0}^{-1}} & & \downarrow{\scriptstyle \eta_{m,1}^{-1}} & & \downarrow{\scriptstyle \eta_{m,2}^{-1}} & & \downarrow{\scriptstyle \eta_{m,3}^{-1}} \\
Z_h^{m,0} & \xrightarrow{\mathbf{grad}^m} & Z_h^{m,1} & \xrightarrow{\mathbf{curl}^m} & Z_h^{m,2} & \xrightarrow{\mathrm{div}^m} & Z_h^{m,3}
\end{array}$$

Proof. The proof is a direct consequence of Lemmas 3–5. For example, we have

that

$$\begin{aligned}
\breve{\mathbf{\Pi}}^2(\mathbf{curl}^m\,\boldsymbol{u}) &= \Big(\boldsymbol{\eta}_{2,\,m}^{-1}\circ\big(\mathbf{\Pi}^{1*}\times\Pi^2\big)\circ\boldsymbol{\eta}_{2,\,m}\circ\mathbf{curl}^m\Big)\boldsymbol{u}\\
&= \Big(\boldsymbol{\eta}_{2,\,m}^{-1}\circ\big(\mathbf{\Pi}^{1*}\times\Pi^2\big)\circ\mathbf{C}\circ\boldsymbol{\eta}_{1,\,m}\Big)\boldsymbol{u} && \text{Lemma 3}\\
&= \Big(\boldsymbol{\eta}_{2,\,m}^{-1}\circ\mathbf{C}\circ\big(\mathbf{\Pi}^{1}\times\Pi^0\big)\circ\boldsymbol{\eta}_{1,\,m}\Big)\boldsymbol{u} && \text{Lemma 5}\\
&= \Big(\mathbf{curl}^m\circ\boldsymbol{\eta}_{1,\,m}^{-1}\circ\big(\mathbf{\Pi}^{1}\times\Pi^0\big)\circ\boldsymbol{\eta}_{1,\,m}\Big)\boldsymbol{u} && \text{Lemma 4}\\
&= \mathbf{curl}^m\left(\breve{\mathbf{\Pi}}^1\boldsymbol{u}\right)
\end{aligned}$$

□

Another important property that can be deduced from the spaces in Cartesian coordinates is the exactness of the discrete sequence:

Theorem 1. *The discrete sequence*

$$0\longrightarrow Z_h^{m,\,0}\xrightarrow{\mathbf{grad}^m} Z_h^{m,\,1}\xrightarrow{\mathbf{curl}^m} Z_h^{m,\,2}\xrightarrow{\mathrm{div}^m} Z_h^{m,\,3}\longrightarrow 0$$

is exact.

Proof. If $u_h\in Z_h^{m,\,3}$, then $\widetilde{u}_h\in Y_h^2$. So the function

$$\boldsymbol{v}_h=\eta_{m,\,2}^{-1}\Big(\big(\mathbf{0}^T,\,-\widetilde{u}_h\big)^T\Big)\in Z_h^{m,\,2}$$

is such that $\mathrm{div}^m\,\boldsymbol{v}_h=u_h$. Similarly, if $\boldsymbol{u}_h\in Z_h^{m,\,2}$ is such that $\mathrm{div}^m\,\boldsymbol{u}_h=\mathbf{0}$, we have that

$$0=\mathrm{div}^m\,\boldsymbol{u}_h=\mathrm{div}_\star^m\,\widetilde{\boldsymbol{u}}_h=\mathrm{div}\,\widetilde{\boldsymbol{u}}_{h,\,\rho z}-\widetilde{u}_{h,\,\theta}\ ,$$

with $\widetilde{u}_{h,\,\theta}\in Y_h^2$. Choosing

$$\boldsymbol{v}_h=\eta_{m,\,1}^{-1}\left(\begin{bmatrix}\mathbf{P}\widetilde{\boldsymbol{u}}_{h,\,\rho z}\\ 0\end{bmatrix}\right)\in Z_h^{m,\,1}$$

we have that

$$\begin{aligned}
\mathbf{curl}^m\,\boldsymbol{v}_h=\eta_{m,\,2}^{-1}(\boldsymbol{C}\widetilde{\boldsymbol{v}}_h)&=\eta_{m,\,2}^{-1}\left(\begin{bmatrix}-\mathbf{P}\mathbf{P}\widetilde{\boldsymbol{u}}_{h,\,\rho z}\\ -\,\mathrm{curl}\,(\mathbf{P}\widetilde{\boldsymbol{u}}_{h,\,\rho z})\end{bmatrix}\right)\\
&=\eta_{m,\,2}^{-1}\left(\begin{bmatrix}\widetilde{\boldsymbol{u}}_{h,\,\rho z}\\ \mathrm{div}\,\widetilde{\boldsymbol{u}}_{h,\,\rho z}\end{bmatrix}\right)=\eta_{m,\,2}^{-1}\left(\begin{bmatrix}\widetilde{\boldsymbol{u}}_{h,\,\rho z}\\ \widetilde{u}_{h,\,\theta}\end{bmatrix}\right)=\boldsymbol{u}_h\ .
\end{aligned}$$

If $\boldsymbol{u}_h\in Z_h^{m,\,1}$ is such that $\mathbf{curl}^m\,\boldsymbol{u}_h=\mathbf{0}$, it follows that $\mathbf{curl}_\star^m\,\widetilde{\boldsymbol{u}}_h=\mathbf{0}$ and so that (see (18)) $-\mathbf{P}\widetilde{\boldsymbol{u}}_{h,\,\rho z}=\mathbf{rot}\,\widetilde{u}_{h,\,\theta}=\mathbf{P}\,\mathbf{grad}\,\widetilde{u}_{h,\,\theta}$. These previous relations imply that the third component is identically null. Moreover, we can also see that $\widetilde{\boldsymbol{u}}_{h,\,\rho z}=-\,\mathbf{grad}\,\widetilde{u}_{h,\,\theta}$ so, choosing $v_h=\eta_{m,\,0}^{-1}(-\widetilde{u}_{h,\,\theta})$ we have that $\mathbf{grad}^m\,v_h=\boldsymbol{u}_h$. Finally, we see that the equation corresponding to the third component in $\mathbf{grad}^m\,u_h=\mathbf{0}$ implies that $u_h\equiv 0$. □

In order to prove error estimates, let us define the following spaces:

$$
\begin{aligned}
H^s_\rho(\widetilde{\mathbf{grad}}^m) =& \Big\{ u \in H(\mathbf{grad}^m) : \eta_{m,0}(u) \in H^s_\rho,\ \widetilde{\mathbf{grad}}^m u \in H^s_\rho \Big\},\\
H^s_\rho(\widetilde{\mathbf{curl}}^m) =& \Big\{ \boldsymbol{u} \in H(\mathbf{curl}^m) : \eta_{m,1}(\boldsymbol{u}) \in H^s_\rho,\ \widetilde{\mathbf{curl}}^m \boldsymbol{u} \in H^s_\rho \Big\},\\
H^s_\rho(\widetilde{\mathrm{div}}^m) =& \Big\{ \boldsymbol{u} \in H(\mathrm{div}^m) : \eta_{m,2}(\boldsymbol{u}) \in H^s_\rho,\ \widetilde{\mathrm{div}}^m \boldsymbol{u} \in H^s_\rho \Big\}\ ,
\end{aligned}
$$

where

$$
\begin{aligned}
\widetilde{\mathbf{grad}}^m u &= \eta_{m,1}(\mathbf{grad}^m u)\ ,\\
\widetilde{\mathbf{curl}}^m \boldsymbol{u} &= \eta_{m,2}(\mathbf{curl}^m \boldsymbol{u})\ ,\\
\widetilde{\mathrm{div}}^m \boldsymbol{u} &= \eta_{m,3}(\mathrm{div}^m \boldsymbol{u}).
\end{aligned}
$$

The proof of the following estimates is analogous to the one in [9, Theorem 4.1].

Lemma 7. *For $s \geq 0$, we have the error estimates*

$$
\Big\| u - \breve{\Pi}^0 u \Big\|_{H(\mathbf{grad}^m)} \leq C h^s \Big(\|\eta_{m,0}(u)\|_{H^{2+s}_\rho} + \|\eta_{m,1}(\mathbf{grad}^m u)\|_{H^{2+s}_\rho} \Big), \qquad u \in H^{s+2}_\rho(\widetilde{\mathbf{grad}}^m), \tag{26}
$$

$$
\Big\| \boldsymbol{u} - \breve{\Pi}^1 \boldsymbol{u} \Big\|_{H(\mathbf{curl}^m)} \leq C h^s \Big(\|\eta_{m,1}(\boldsymbol{u})\|_{H^{2+s}_\rho} + \|\eta_{m,2}(\mathbf{curl}^m \boldsymbol{u})\|_{H^{2+s}_\rho} \Big), \qquad \boldsymbol{u} \in H^{s+2}_\rho(\widetilde{\mathbf{curl}}^m), \tag{27}
$$

$$
\Big\| \boldsymbol{u} - \breve{\Pi}^2 \boldsymbol{u} \Big\|_{\boldsymbol{H}(\mathrm{div}^m)} \leq C h^s \Big(\|\eta_{m,2}(\boldsymbol{u})\|_{H^{2+s}_\rho} + \|\eta_{m,3}(\mathrm{div}^m \boldsymbol{u})\|_{H^{2+s}_\rho} \Big), \qquad \boldsymbol{u} \in H^{s+2}_\rho(\widetilde{\mathrm{div}}^m), \tag{28}
$$

$$
\Big\| u - \breve{\Pi}^3 u \Big\|_{L^2_\rho} \leq C h^s \|u\|_{H^{2+s}_\rho} \qquad u \in H^{s+2}_\rho. \tag{29}
$$

Proof. Since the domain is bounded we have that $0 < \rho < R$. Moreover, the continuous embedding $H^{s+2}_\rho \hookrightarrow H^s$ holds [8] and so, for $s \geq 2$ we have that $H^s_\rho(\widetilde{\mathbf{grad}}^m) \subset \widetilde{Z}^{m,0}$, $H^s_\rho(\widetilde{\mathbf{curl}}^m) \subset \widetilde{Z}^{m,1}$, $H^s_\rho(\widetilde{\mathrm{div}}^m) \subset \widetilde{Z}^{m,2}$ and $H^s_\rho \subset \widetilde{Z}^{m,3}$. The procedure to derive the estimates is analogous for all the cases and can be

summarized as follows, for $k = 1, 2, 3$:

$$\begin{aligned}
\left\| u - \breve{\Pi}^k u \right\|_\rho &= \left\| u - \left(\eta_{m,\,k}^{-1} \circ \Pi^k \circ \eta_{m,\,k} \right) u \right\|_\rho \\
&= \left\| \left(\eta_{m,\,k}^{-1} \circ \eta_{m,\,k} \right) u - \left(\eta_{m,\,k}^{-1} \circ \Pi^k \circ \eta_{m,\,k} \right) u \right\|_\rho \\
&= \left\| \eta_{m,\,k}^{-1} \Big(\eta_{m,\,k}(u) - \Pi^k(\eta_{m,\,k}(u)) \Big) \right\|_\rho \\
&\leq C \left\| \eta_{m,\,k}^{-1} \Big(\eta_{m,\,k}(u) - \Pi^k(\eta_{m,\,k}(u)) \Big) \right\| \\
&\leq C \left\| \eta_{m,\,k}(u) - \Pi^k(\eta_{m,\,k}(u)) \right\| \\
&\leq C\, h^s \, \| \eta_{m,\,k}(u) \|_{H^s} \\
&\leq C\, h^s \, \| \eta_{m,\,k}(u) \|_{H_\rho^{s+2}} \ ,
\end{aligned}$$

where the constant C is different for each inequality, but is independent of u and can depends on h only through the ratio between the biggest and the smallest element h_{max}/h_{min}. The estimates for the terms involving the differential operators are reduced to the previous ones exploiting the commutativity of the projectors. Consider $u \in H_\rho^{s+2}$, we have that

$$\begin{aligned}
\left\| u - \breve{\Pi}^3 u \right\|_\rho &\leq \left\| \sqrt{\frac{R}{\rho}} \left(u - \Pi^2 u \right) \right\|_\rho = \sqrt{R} \left\| u - \Pi^2 u \right\| \\
&\leq \sqrt{R}\, C\, h^s \, \| u \|_{H^s} \leq \widetilde{C} h^s \, \| u \|_{H_\rho^{s+2}} \ .
\end{aligned}$$

This proves (29).
Considering a function $u \in H_\rho^{s+2}(\widetilde{\mathbf{grad}}^{\,m})$, it follows

$$\begin{aligned}
\left\| u - \breve{\Pi}^0 u \right\|_\rho &= \left\| u - \frac{\rho}{m} \Pi^0 \left(\frac{m}{\rho} u \right) \right\|_\rho \\
&= \left\| \frac{\rho}{m} \left(\frac{m}{\rho} u \right) - \Pi^0 \left(\frac{m}{\rho} u \right) \right\|_\rho \\
&\leq R \left\| \frac{m}{\rho} u - \Pi^0 \left(\frac{m}{\rho} u \right) \right\|_\rho \leq C h^s \left\| \frac{m}{\rho} u \right\|_{H_\rho^{s+2}} .
\end{aligned}$$

So, we have that

$$\left\| u - \breve{\Pi}^0 u \right\|_\rho \leq C h^s \left\| \frac{m}{\rho} u \right\|_{H_\rho^{s+2}} = C h^s \, \| \eta_{m,\,0}(u) \|_{H_\rho^{s+2}} \ . \tag{30}$$

Consider now a function $\boldsymbol{u} \in H_\rho^{s+2}(\widetilde{\mathrm{div}}^{\,m})$, the estimate (28) involves the norm

$$\| \boldsymbol{u} \|^2_{H_\rho(\mathrm{div}^m)} = \| \boldsymbol{u} \|^2_{L^2_\rho} + \| \mathrm{div}^m \, \boldsymbol{u} \|^2_{L^2_\rho} .$$

For the first term we have that

$$\left\|\boldsymbol{u}-\breve{\Pi}^2\boldsymbol{u}\right\|_\rho^2=\left\|\boldsymbol{u}_{\rho z}-\Pi^{1*}\boldsymbol{u}_{\rho z}\right\|_\rho^2 + \left\|u_\theta-\frac{\rho}{m}\Pi^2\left(\frac{m\,u_\theta-u_\rho}{\rho}\right)-\frac{1}{m}\left[\Pi^{1*}\boldsymbol{u}_{\rho z}\right]_\rho\right\|_\rho^2$$

adding and subtracting $\frac{u_\rho}{m}$ in the second term we obtain

$$\begin{aligned}
&\leq \left\|\boldsymbol{u}_{\rho z}-\Pi^{1*}\boldsymbol{u}_{\rho z}\right\|_\rho^2\\
&+2\left\|\frac{\rho}{m}\left(\frac{m\,u_\theta-u_\rho}{\rho}-\Pi^2\left(\frac{m\,u_\theta-u_\rho}{\rho}\right)\right)\right\|_\rho^2\\
&+2\left\|\frac{1}{m}\left(u_\rho-\left[\Pi^{1*}\boldsymbol{u}_{\rho z}\right]_\rho\right)\right\|_\rho^2\\
&\leq 3\left\|\boldsymbol{u}_{\rho z}-\Pi^{1*}\boldsymbol{u}_{\rho z}\right\|_\rho^2+R^2\left\|\left(\widetilde{u}_\theta-\Pi^2\widetilde{u}_\theta\right)\right\|_\rho^2\\
&\leq Ch^{2s}\left(\|\boldsymbol{u}\|_{H^{s+2}_\rho}^2+\|\widetilde{u}\|_{H^{s+2}_\rho}^2\right)=Ch^{2s}\left\|\eta_{m,\,2}(\boldsymbol{u})\right\|_{H^{s+2}_\rho}^2.
\end{aligned}$$

We are left with

$$\left\|\boldsymbol{u}-\breve{\Pi}^2\boldsymbol{u}\right\|_{L^2_\rho}\leq Ch^s\left\|\eta_{m,\,2}(\boldsymbol{u})\right\|_{H^{s+2}_\rho}. \tag{31}$$

The estimate for $\|\mathrm{div}^m\,\boldsymbol{u}\|_\rho^2$ follows from the commutativity of the projectors and (29):

$$\left\|\mathrm{div}^m\left(\boldsymbol{u}-\breve{\Pi}^2\boldsymbol{u}\right)\right\|_\rho=\left\|\mathrm{div}^m\,\boldsymbol{u}-\breve{\Pi}^3(\mathrm{div}^m\,\boldsymbol{u})\right\|_\rho\leq Ch^s\left\|\mathrm{div}^m\,\boldsymbol{u}\right\|_{H^{s+2}_\rho}.$$

This concludes the proof of (28). The estimate (27) is proven analogously, considering the norm

$$\|\boldsymbol{u}\|^2_{H_\rho(\mathbf{curl}^m)}=\|\boldsymbol{u}\|^2_{L^2_\rho}+\|\mathbf{curl}^m\,\boldsymbol{u}\|^2_{L^2_\rho}.$$

For the first term we have that

$$\left\|\boldsymbol{u}-\breve{\Pi}^1\boldsymbol{u}\right\|_\rho^2=\left\|u_\theta-\Pi^0u_\theta\right\|_\rho^2 + \left\|\boldsymbol{u}_{\rho z}-\frac{\rho}{m}\Pi^1(\widetilde{\boldsymbol{u}}_{\rho z})-\frac{1}{m}\begin{bmatrix}\Pi^0u_\theta\\0\end{bmatrix}\right\|_\rho^2$$

adding and subtracting $\left(\frac{u_\theta}{m},\,0\right)^T$ in the second term we obtain

$$\begin{aligned}
&\leq \left\|u_\theta-\Pi^0u\theta\right\|_\rho^2\\
&+2\left\|\frac{\rho}{m}\left(\widetilde{\boldsymbol{u}}_{\rho z}-\Pi^1(\widetilde{\boldsymbol{u}}_{\rho z})\right)\right\|_\rho^2+2\left\|u_\theta-\Pi^0u_\theta\right\|_\rho^2\\
&\leq Ch^{2s}\left(\|u_\theta\|_{H^{s+2}_\rho}^2+\|\widetilde{\boldsymbol{u}}_{\rho z}\|_{H^{s+2}_\rho}^2\right)=Ch^{2s}\left\|\eta_{m,\,1}(\boldsymbol{u})\right\|_{H^{s+2}_\rho}^2.
\end{aligned}$$

So we have that

$$\left\| \boldsymbol{u} - \breve{\Pi}^1 \boldsymbol{u} \right\|_{L^2_\rho} \leq C h^s \left\| \eta_{m,\,1}(\boldsymbol{u}) \right\|_{H^{s+2}_\rho} .$$

The estimate for $\|\mathbf{curl}^m \boldsymbol{u}\|^2_\rho$ follows from the commutativity of the projectors and (31):

$$\begin{aligned} \left\| \mathbf{curl}^m \left(\boldsymbol{u} - \breve{\Pi}^1 \boldsymbol{u} \right) \right\|_\rho &= \left\| \mathbf{curl}^m \boldsymbol{u} - \breve{\Pi}^2 (\mathbf{curl}^m \boldsymbol{u}) \right\|_\rho \\ &\leq C h^s \left\| \eta_{m,\,2}(\mathbf{curl}^m \boldsymbol{u}) \right\|_{H^{s+2}_\rho} . \end{aligned}$$

This conclude the proof of (27). Consider a function $u \in H^{s+2}_\rho(\widetilde{\mathbf{grad}}^m)$, the norm involved in (26) is

$$\|u\|^2_{H_\rho(\mathbf{grad}^m)} = \|u\|^2_{L^2_\rho} + \|\mathbf{grad}^m u\|^2_{L^2_\rho} .$$

For the first term, we already have the estimate given by (30). The estimate for the second term follows from the commutativity property of the projectors and (31):

$$\begin{aligned} \left\| \mathbf{grad}^m \left(u - \breve{\Pi}^0 u \right) \right\|_\rho &= \left\| \mathbf{grad}^m u - \breve{\Pi}^1 (\mathbf{grad}^m u) \right\|_\rho \\ &\leq C h^s \left\| \eta_{m,\,1}(\mathbf{grad}^m u) \right\|_{H^{s+2}_\rho} . \end{aligned}$$

This concludes the proof of (26). □

4 IsoGeometric Analysis

In this section we briefly introduce the basic concepts of IsoGeometric Analysis following [20]. We will start with the definition of Basis splines (B-splines) on a reference two-dimensional domain $\widehat{S}$ in the univariate case and then we introduce its extension, via tensor product, to the multivariate case.

Considering an exact de Rham complex of continuous spaces defined in the reference domain, we then define the corresponding conforming discrete B-spline spaces and projectors and we show that they form a commuting diagram. We will consider a regular parametrization of the two-dimensional physical domain, which will be the cross-section of our axisymmetric domain S, described by a B-spline or by a Non-Uniform Rational Basis Spline (NURBS) surface. All the results valid on the parametric domain can be extended to the case of the physical one and error estimates like (14) hold.

We start defining the so-called knot vector $\boldsymbol{\Xi}$, which is a sequence of ordered real numbers that we assume, without loss of generality, bounded by 0 and 1. In this work we will consider only open knot vectors, which are characterized by the fact that the first $p+1$ knots are equal to 0 and the last $p+1$ knots are equal to 1, *i.e.*

$$\boldsymbol{\Xi} = \{\xi_1 = \ldots = \xi_{p+1} < \ldots < \xi_{n+1} = \ldots = \xi_{n+p+1}\} ,$$

where p is the degree and n is the number of the B-spline polynomials. B-spline polynomials are the fundamental functions used to define our finite-dimensional spaces and can be defined recursively using the well known Cox-DeBoor formula: starting from piecewise constant polynomials ($p = 0$)

$$\widehat{B}_i^0(\zeta) = \begin{cases} 1 & \xi_i \leq \zeta < \xi_{i+1} \\ 0 & \text{otherwise} \end{cases} ,$$

the higher degree polynomials ($p \geq 1$) are defined by

$$\widehat{B}_i^p(\zeta) = \frac{\zeta - \xi_i}{\xi_{i+p} - \xi_i} \widehat{B}_i^{p-1}(\zeta) + \frac{\xi_{i+p+1} - \zeta}{\xi_{i+p+1} - \xi_{i+1}} \widehat{B}_{i+1}^{p-1}(\zeta) ,$$

with the convention that $0/0$ is equal to 0. This formula generates a set of n B-spline which has many favorable properties. In particular, these functions are non-negative, form a partition of unity and have local support. Moreover, the support the i-th B-spline is contained in the interval $[\xi_i, \xi_{i+p+1}]$, so the size of the support is reduced by knot repetitions (see Figure 2):

$$\widehat{B}_i^p(\zeta) = 0 , \qquad \zeta \notin [\xi_i, \xi_{i+p+1}] .$$

Conversely, in each interval $[\xi_j, \xi_{j+1}]$ there are exactly $p + 1$ B-splines which are different from 0:

$$\widehat{B}_i^p(\zeta) = 0 , \qquad \zeta \in [\xi_j, \xi_{j+1}],\, i \notin \{j, j-1, \ldots, j-p\} .$$

It is possible to describe the knot vector $\boldsymbol{\Xi}$ using other two vectors: a vector containing the knots without repetition, that we indicate with $\boldsymbol{\zeta} \in \mathbb{R}^\ell$, and a vector containing the number of times each knot is repeated $1 \leq r_i \leq p$, $2 \leq i \leq \ell - 1$, with $r_1 = r_\ell = p + 1$. The number $\alpha_i = p - r_i$ denotes the regularity of the B-spline function at the knot ζ_i. In analogy to the standard Finite Element Method (FEM), we can use $\boldsymbol{\zeta}$ to define elements of a mesh with the corresponding mesh size $h_i = \zeta_{i+1} - \zeta_i,\ 1 \leq i \leq \ell - 1$. We say that the partition defined by $\boldsymbol{\zeta}$ is locally quasi uniform if there exists a constant $\eta \geq 1$ such that

$$\eta^{-1} \leq \frac{h_i}{h_{i+1}} \leq \eta, \qquad 1 \leq i \leq \ell - 2.$$

We can now define the spline spaces [18, 13] as

$$S_{\boldsymbol{\alpha}}^p(\boldsymbol{\zeta}) = \text{span}\left\{ \widehat{B}_i^p,\, i = 1, \ldots, n \right\} .$$

Note that spline space can be completely characterized either by the knot vector $\boldsymbol{\Xi}$ or by the degree p, the mesh $\boldsymbol{\zeta}$ and the regularity $\boldsymbol{\alpha}$ (or the knot repetitions). Figure 2 shows two sets of quadratic B-spline basis functions generated by two different knot vectors with the same elements but different regularity. The multivariate spaces are

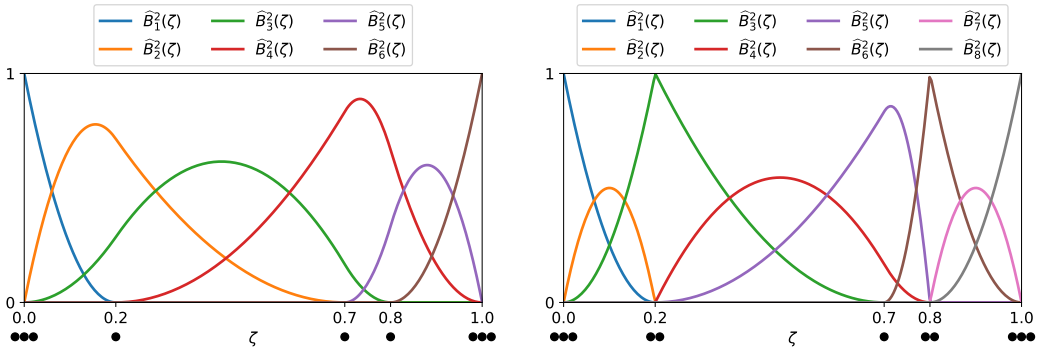

Figure 2: Two set of quadratic B-spline basis functions generated by knot vectors including the same points with different multiplicities. The dots below the ζ-axis indicate the knot repetitions. Note that the support of the less regular B-splines (right) is smaller that the ones with higher regularity (left).

simply defined via tensor product. We will explicitly introduce the quantities in the two-dimensional case, since it is the most relevant for this work. Let $\boldsymbol{\Xi}_1$ and $\boldsymbol{\Xi}_2$ be two locally quasi uniform open knot vectors corresponding to parametric directions. The associated shape-regular Bezier mesh on $\widehat{S} = (0,\,1)^2$ is given by

$$\widehat{\mathcal{Q}}_h = \{Q = (\zeta_i,\,\zeta_{i+1}) \times (\zeta_j,\,\zeta_{j+1}),\, 1 \leq i \leq \ell_1,\; 1 \leq j \leq \ell_2\},$$

where $h = \max\left\{\mathrm{diam}(Q),\, Q \in \widehat{\mathcal{Q}}_h\right\}$ is the global mesh size. We will denote the coarsest mesh $\widehat{\mathcal{Q}}_0$ with the subscript 0. From the univariate B-spline basis functions $\widehat{B}_{i,\,d}$ defined by $\boldsymbol{\Xi}_d$, $d = 1, 2$, we define the tensor product basis functions on $\widehat{S}$:

$$\widehat{B}^{p_1,\,p_2}_{ij} = \widehat{B}^{p_1}_{i,\,1} \otimes \widehat{B}^{p_2}_{j,\,2}, \qquad 1 \leq i \leq n_1,\, 1 \leq j \leq n_2$$

and the spline space is analogously defined as:

$$S^{p_1,\,p_2}_{\boldsymbol{\alpha}_1,\,\boldsymbol{\alpha}_2}\left(\widehat{\mathcal{Q}}_h\right) = \mathrm{span}\left\{\widehat{B}^{p_1,\,p_2}_{ij},\, 1 \leq i \leq n_1,\, 1 \leq j \leq n_2\right\}.$$

We also define a generalization of B-splines, called NURBS, which is particularly useful to describe the geometry since it allows to exactly represent conic sections. Given set of weights $w_{ij} \geq 0$, $1 \leq i \leq n_1$, $1 \leq j \leq n_2$ thaat sum to one, NURBS are defined by

$$\widehat{N}^{p_1,\,p_2}_{ij} = \frac{w_{ij}\widehat{B}^{p_1,\,p_2}_{ij}}{\sum_{k,\ell} w_{k\ell}\widehat{B}^{p_1,\,p_2}_{k\ell}}.$$

Gathering the weights in a vector $\mathbf{W}$ we define the associated NURBS space:

$$N^{p_1,\,p_2}_{\boldsymbol{\alpha}_1,\,\boldsymbol{\alpha}_2}\left(\widehat{\mathcal{Q}}_h, \mathbf{W}\right) = \mathrm{span}\left\{\widehat{N}^{p_1,\,p_2}_{ij},\, 1 \leq i \leq n_1,\, 1 \leq j \leq n_2\right\}.$$

It is now possible to introduce the following B-spline vector spaces defined on the reference domain $\widehat{S}$:

$$\begin{aligned}
\widehat{Y}_h^0 &= S^{p_1,p_2}_{\boldsymbol{\alpha}_1,\boldsymbol{\alpha}_2}\Big(\widehat{\mathcal{Q}}_h\Big),\\
\widehat{Y}_h^1 &= S^{p_1-1,p_2}_{\boldsymbol{\alpha}_1-1,\boldsymbol{\alpha}_2}\Big(\widehat{\mathcal{Q}}_h\Big) \times S^{p_1,p_2-1}_{\boldsymbol{\alpha}_1,\boldsymbol{\alpha}_2-1}\Big(\widehat{\mathcal{Q}}_h\Big),\\
\widehat{Y}_h^{1*} &= S^{p_1,p_2-1}_{\boldsymbol{\alpha}_1,\boldsymbol{\alpha}_2-1}\Big(\widehat{\mathcal{Q}}_h\Big) \times S^{p_1-1,p_2}_{\boldsymbol{\alpha}_1-1,\boldsymbol{\alpha}_2}\Big(\widehat{\mathcal{Q}}_h\Big),\\
\widehat{Y}_h^2 &= S^{p_1-1,p_2-1}_{\boldsymbol{\alpha}_1-1,\boldsymbol{\alpha}_2-1}\Big(\widehat{\mathcal{Q}}_h\Big).
\end{aligned} \tag{32}$$

These are the discrete conforming counterparts of the spaces

$$\begin{aligned}
\widehat{Y}^0 &= H(\widehat{\mathbf{grad}};\,\widehat{S}) = \Big\{u \in L^2(\widehat{S}) : \widehat{\mathbf{grad}}\,u \in L^2(\widehat{S};\mathbb{R}^2)\Big\},\\
\widehat{Y}^1 &= H(\widehat{\mathrm{curl}};\,\widehat{S}) \;= \Big\{\boldsymbol{u} \in L^2(\widehat{S};\mathbb{R}^2) : \widehat{\mathrm{curl}}\,\boldsymbol{u} \in L^2(\widehat{S})\Big\},\\
\widehat{Y}^{1*} &= H(\widehat{\mathrm{div}};\,\widehat{S}) \;= \Big\{\boldsymbol{u} \in L^2(\widehat{S};\mathbb{R}^2) : \widehat{\mathrm{div}}\,\boldsymbol{u} \in L^2(\widehat{S})\Big\},\\
\widehat{Y}^2 &= L^2(\widehat{S}).
\end{aligned}$$

Following [19], it is then possible to define a set of projectors $\widehat{\Pi}^k$, $k = 0, 1, 1*, 2$ such that the following diagrams are commutative

$$\begin{array}{ccccccccc}
\mathbb{R} & \longrightarrow & \widehat{Y}^0 & \xrightarrow{\widehat{\mathbf{grad}}} & \widehat{Y}^1 & \xrightarrow{\widehat{\mathrm{curl}}} & \widehat{Y}^2 & \longrightarrow & 0\\
 & & \downarrow{\scriptstyle \widehat{\Pi}^0} & & \downarrow{\scriptstyle \widehat{\Pi}^1} & & \downarrow{\scriptstyle \widehat{\Pi}^2} & & \\
\mathbb{R} & \longrightarrow & \widehat{Y}_h^0 & \xrightarrow{\widehat{\mathbf{grad}}} & \widehat{Y}_h^1 & \xrightarrow{\widehat{\mathrm{curl}}} & \widehat{Y}_h^2 & \longrightarrow & 0
\end{array}$$

$$\begin{array}{ccccccccc}
\mathbb{R} & \longrightarrow & \widehat{Y}^0 & \xrightarrow{\widehat{\mathbf{rot}}} & \widehat{Y}^{1*} & \xrightarrow{\widehat{\mathrm{div}}} & \widehat{Y}^2 & \longrightarrow & 0\\
 & & \downarrow{\scriptstyle \widehat{\Pi}^0} & & \downarrow{\scriptstyle \widehat{\Pi}^{1*}} & & \downarrow{\scriptstyle \widehat{\Pi}^2} & & \\
\mathbb{R} & \longrightarrow & \widehat{Y}_h^0 & \xrightarrow{\widehat{\mathbf{rot}}} & \widehat{Y}_h^{1*} & \xrightarrow{\widehat{\mathrm{div}}} & \widehat{Y}_h^2 & \longrightarrow & 0
\end{array}$$

Once that the spaces are defined on the parametric domain, we turn our attention to the physical domain S, which we assume to be represented as $S = \boldsymbol{F}(\widehat{S})$, where the parametrization $\boldsymbol{F}$ is a NURBS surface generated by a given set of control points, which are the coefficients multiplying the basis functions, see Figure 3. Given a mesh $\widehat{\mathcal{Q}}_h$ on the reference domain, the parametrization induces a mesh in the physical one:

$$\mathcal{Q}_h = \Big\{K \subset S :\, K = \boldsymbol{F}(Q),\, Q \in \widehat{\mathcal{Q}}_h\Big\}.$$

We assume that the parametrization $\boldsymbol{F}$ is regular in the sense of [20, Assumption 3.1], that is, we assume that it is a bi-Lipschitz homeomorphism between $\widehat{S}$ and S, $\boldsymbol{F}|_{\overline{Q}} \in C^\infty(\overline{Q})$, $\overline{Q} \in \widehat{\mathcal{Q}}_0$ and $\boldsymbol{F}^{-1}\big|_{\overline{K}} \in C^\infty(\overline{K})$, $\overline{K} \in \mathcal{Q}_0$. With the introduced

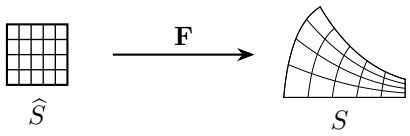

Figure 3: Geometry mapping from reference domain.

parametrization, the following pullbacks that relate spaces on the physical domain to the corresponding ones in the parametric domain are well-defined:

$$\begin{aligned}
\iota^0 &: Y^0 \to \widehat{Y}^0, && v \mapsto v \circ \boldsymbol{F} \ , \\
\iota^1 &: Y^1 \to \widehat{Y}^1, && \boldsymbol{v} \mapsto {J_{\boldsymbol{F}}}^T (\boldsymbol{v} \circ \boldsymbol{F}) \ , \\
\iota^{1*} &: Y^{1*} \to \widehat{Y}^{1*}, && \boldsymbol{v} \mapsto \det(J_{\boldsymbol{F}}) {J_{\boldsymbol{F}}}^{-1} (\boldsymbol{v} \circ \boldsymbol{F}) \ , \\
\iota^2 &: Y^2 \to \widehat{Y}^2, && v \mapsto \det(J_{\boldsymbol{F}}) (v \circ \boldsymbol{F}) \ .
\end{aligned} \tag{33}$$

The discrete spaces on the physical domain are defined by push-forward, *i.e.* applying the inverse of (33) to the discrete spaces on the reference domain (32):

$$\begin{aligned}
Y_h^0 &= \left\{ v_h : \iota^0(v_h) \in \widehat{Y}_h^0 \right\}, \\
Y_h^1 &= \left\{ \boldsymbol{v}_h : \iota^1(\boldsymbol{v}_h) \in \widehat{Y}_h^1 \right\}, \\
Y_h^{1*} &= \left\{ \boldsymbol{v}_h : \iota^{1*}(\boldsymbol{v}_h) \in \widehat{Y}_h^{1*} \right\}, \\
Y_h^2 &= \left\{ v_h : \iota^2(v_h) \in \widehat{Y}_h^2 \right\}.
\end{aligned}$$

Moreover, we assume that the regularity of the parametrization $\boldsymbol{F}$ is higher or equal to the one of the discrete spaces (32) [18]. Between the continuous and the discrete spaces it is possible to define stable projectors such that the diagrams (12) and (13) are commuting. Finally, the following estimates hold (2D analogous of [20, Corollary 5.12]):

$$\begin{aligned}
&\left\| u - \Pi^0 u \right\|_{H^1(S)} \leq C h^s \left\| u \right\|_{H^{s+1}(S)} , && u \in H^{s+1}(S), \\
&\left\| \boldsymbol{u} - \Pi^1 \boldsymbol{u} \right\|_{H(\mathrm{curl};\, S)} \leq C h^s \left\| \boldsymbol{u} \right\|_{H^s(\mathrm{curl};\, S)} , && \boldsymbol{u} \in H^s(\mathrm{curl};\, S), \\
&\left\| \boldsymbol{u} - \Pi^{1*} \boldsymbol{u} \right\|_{H(\mathrm{div};\, S)} \leq C h^s \left\| \boldsymbol{u} \right\|_{H^s(\mathrm{div};\, S)} , && \boldsymbol{u} \in H^s(\mathrm{div};\, S), \\
&\left\| u - \Pi^2 u \right\|_{L^2(S)} \leq C h^s \left\| u \right\|_{H^s(S)} , && u \in H^s(S).
\end{aligned}$$

5 Numerical experiments

We present the results of several numerical experiments carried out with the discretization described in the previous sections.

5.1 Source problem

In this test case we consider the problem of reconstructing the magnetic flux $\boldsymbol{B}$ in a stationary case on an axisymmetric domain whose cross-section is depicted in Figure 4 (left). To do so, we employ the so-called $\boldsymbol{A}$-formulation, already intro-

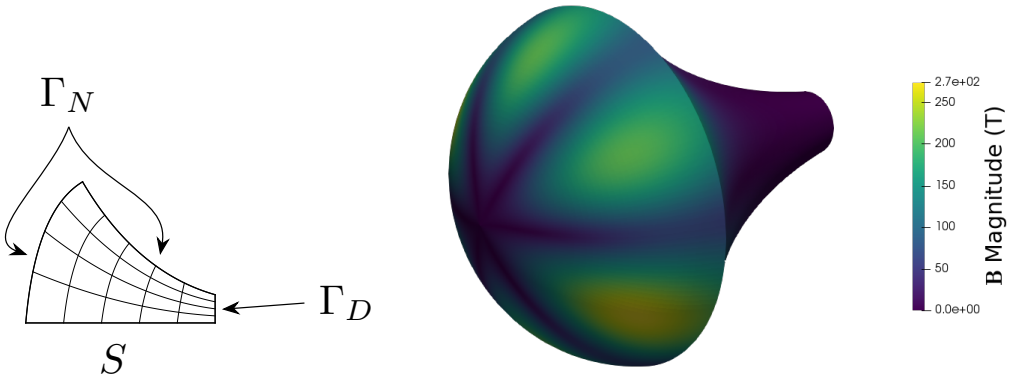

Figure 4: Section of the computational domain with the boundaries associated to Σ_N (Γ_N) and Σ_D (Γ_D) (left) and magnitude of the magnetic flux density $\boldsymbol{B}$ on the domain (right).

duced in (3), which amounts to compute the vector potential $\boldsymbol{A}$ which can be then related to the flux by $\mathbf{curl}\,\boldsymbol{A} = \boldsymbol{B}$. Notice that the accurate computation of the vector potential is essential in modelling particle tracking in accelerator magnets, as discussed in [10]. Using a Coulomb gauge and imposing homogeneous Dirichlet boundary conditions on Σ_D regularized by the same Coulomb gauge and Neumann boundary conditions on Σ_N, we have that

$$\begin{aligned}
\mathbf{curl}\left(\mu^{-1}\,\mathbf{curl}\,\boldsymbol{A}\right) &= \boldsymbol{j}\ , && \text{in } \breve{\Omega}\ ,\\
\operatorname{div}\left(\epsilon\boldsymbol{A}\right) &= 0\ , && \text{in } \breve{\Omega}\ ,\\
\left(\mu^{-1}\,\mathbf{curl}\,\boldsymbol{A}\right)\times\boldsymbol{\nu} &= \boldsymbol{j}_\Sigma\ , && \text{on } \Sigma_N\ ,\\
\boldsymbol{A}\times\boldsymbol{\nu} &= \mathbf{0}\ , && \text{on } \Sigma_D\ ,\\
\left(\epsilon\boldsymbol{A}\right)\cdot\boldsymbol{\nu} &= 0\ , && \text{on } \Sigma_N\ ,\\
\operatorname{div}\left(\epsilon\boldsymbol{A}\right) &= 0\ , && \text{on } \Sigma_D\ ,
\end{aligned}$$

where $\boldsymbol{j}$ and $\boldsymbol{j}_\Sigma$ are given source and surface current densities, respectively, while ϵ and μ are scalar constants, given by the corresponding values of these quantities in vacuum:

$$\epsilon \approx 8.8542\times10^{-12}\,\mathrm{F\,m^{-1}}\ , \qquad \mu = 4\pi\times10^{-7}\,\mathrm{H\,m^{-1}}\ . \tag{34}$$

Note that, due to the fact that the permeability is constant, the magnetic flux density and the magnetic field strength are related by the simple relation $\boldsymbol{B} = \mu\boldsymbol{H}$.

The method is tested using a manufactured solution which depends on a parameter γ and satisfies the homogeneous Dirichlet conditions on Σ_D:

$$\boldsymbol{A}^{ex} = \begin{bmatrix} \cos(3\theta)\,(5-z)^3\,\rho^{\gamma+1}\,e^{-\rho} \\ \rho^2\,(\sin(\theta) - 2\sin(\theta)^3)\,(5-z)^\gamma \\ \sin(2\theta)\,(1-\cos(5-z))\,\rho^{\gamma+1} \end{bmatrix} .$$

The vector potential $\boldsymbol{A}^{ex}$ is not Coulomb gauged, *i.e.* $\mathrm{div}(\epsilon \boldsymbol{A}^{ex}) \neq 0$ and will be different from the solution of (5.1), but the magnetic induction $\boldsymbol{B} = \mathbf{curl}\,\boldsymbol{A}$, which is represented in Figure 4 (right), is gauge independent and is used to compute the error. A mixed formulation has been used to impose the Coulomb gauge and solve (5.1). Using the method proposed in this work allows to solve a sequence of decoupled two-dimensional problems (one for each Fourier mode m) instead of a full three-dimensional one, with a significant advantage in terms of computational cost. In particular, consider the two finite-dimensional spaces, characterized by their basis functions,

$$\begin{aligned} \mathrm{span}\left(\{b_i\}_{i=1}^{N_0}\right) &= Z^{m,0}_{h,\Gamma_D} \subset Z^{m,0}_{\Gamma_D} = H_\rho(\mathbf{grad}^m) \ , \\ \mathrm{span}\left(\{\boldsymbol{c}_i\}_{i=1}^{N_1}\right) &= Z^{m,1}_{h,\Gamma_D} \subset Z^{m,1}_{\Gamma_D} = H_\rho(\mathbf{curl}^m) \ , \end{aligned}$$

where N_0 and N_1 indicate the dimensions of the corresponding finite-dimensional spaces and the subscript Γ_D denote the boundary on which essential boundary conditions are imposed. Notice that, even if it is not explicit in the notation, the basis functions are different for each value of m. The discrete mixed formulation for problem (5.1) amounts to solving for each value of $m \neq 0$ the following linear system:

$$\begin{bmatrix} \mathbf{A}_m & \mathbf{B}_m \\ \mathbf{B}_m^T & \mathbf{0} \end{bmatrix} \begin{bmatrix} \mathbf{u}_m \\ \mathbf{p}_m \end{bmatrix} = \begin{bmatrix} \mathbf{f}_m \\ \mathbf{0} \end{bmatrix} \tag{35}$$

where $\mathbf{u}_m$ and $\mathbf{p}_m$ are the Degrees of Freedom (DoFs) associated to the discrete solution,

$$\begin{aligned} [\mathbf{A}_m]_{i,\,j} &= \int (\mathbf{curl}^m\,\boldsymbol{c}_j) \cdot (\mathbf{curl}^m\,\boldsymbol{c}_i)\,\rho \mathrm{d}\rho \mathrm{d}z \ , \\ [\mathbf{B}_m]_{i,\,j} &= \int (\mathbf{grad}^m\,b_j) \cdot \boldsymbol{c}_i\,\rho \mathrm{d}\rho \mathrm{d}z \end{aligned}$$

and $\mathbf{f}_m$ is the term associated to the current density and the boundary term. If all the DoFs corresponding to each mode are collected in a single vector $\mathbf{x}$, we end up with a linear system of the form shown in Figure 5, where each matrix $\mathbf{C}_m$ corresponds to that in (35) and $\mathbf{g}$ is obtained by the concatenation of all the right-hand side terms in (35). For this testcase we choose the modes

$$m = \pm 1,\ \pm 2,\ \pm 3 \ ,$$

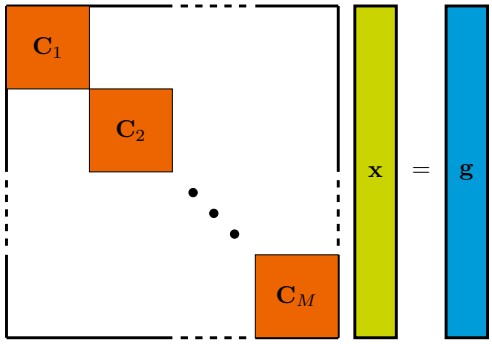

Figure 5: Block diagonal structure of the linear system.

so that $M = 6$. Note that the block diagonal structure in Figure 5 is obtained thanks to the Fourier basis and would not be obtained for a general choice of the basis in the angular direction.

In the left plot of Figure 6, we report the error trend with respect to the number of subdivisions (h-refinement) for a smooth solution ($\gamma = 2$). In this case the

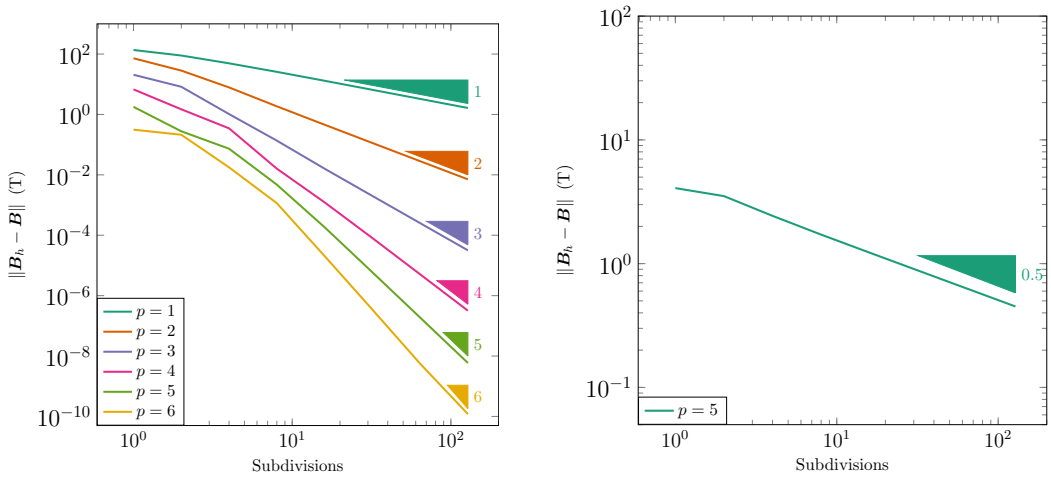

Figure 6: Error on the magnetic field with respect to the number of subdivisions for a regular solution (left, $\gamma = 2$) and for a non-smooth solution (right, $\gamma = 0.5$) which limits the convergence rate.

convergence rate is equal to the polynomial degree p of the basis functions. In the case of a less regular solution with $\gamma = 0.5$, we can see instead in Figure 6 (right) that the low regularity of the solution limits the convergence rate as expected.

5.2 Pillbox cavity

In this section, we apply the method presented in this work to the computation of the eigenvalues for a cylindrical cavity, known in the literature as pillbox cavity [17, §8.7], see Figure 7. Given a pillbox cavity of radius $R = 35\,\text{mm}$ and length $L = 100\,\text{mm}$, we want to compute the eigenvalues and eigenfunctions for the electric field strength $\boldsymbol{E}$, satisfying the equations

$$\begin{aligned} &\mathbf{curl}\left(\mu^{-1}\,\mathbf{curl}\left(\boldsymbol{E}\right)\right) = \omega^2 \epsilon \boldsymbol{E}\ , && \text{in } \breve{\Omega}\ , \\ &\operatorname{div}\left(\epsilon \boldsymbol{E}\right) = \mathbf{0}\ , && \text{in } \breve{\Omega}\ , \\ &\boldsymbol{E} \times \boldsymbol{\nu} = \mathbf{0}\ , && \text{in } \partial\breve{\Omega}\ , \end{aligned} \tag{36}$$

where ω^2 is the eigenvalue associated to the eigenfunction $\boldsymbol{E}$ that we will consider different from 0, $\boldsymbol{\nu}$ indicates the outer unit normal, ϵ and μ are two scalar constants representing, respectively, the permittivity and the permeability in vacuum already defined in (34). Since we consider $\omega^2 \neq 0$, the divergence constraint in (36) is satisfied and can be neglected [21]. The solutions of (36) associated to eigenvalues different from zero can be divided in two classes: one, TM (Transverse Magnetic), is associated to fields where $B_z = 0$ everywhere and $E_z = 0$ on the lateral surface of the cylinder (see Figure 7, left). The second one, TE (Transverse Electric), is associated to fields where $E_z = 0$ everywhere and $\partial_{\boldsymbol{\nu}} B_z = 0$ on the lateral surface of the cylinder see Figure 7, right) [17, Chapter 8]. The corresponding eigenvalues

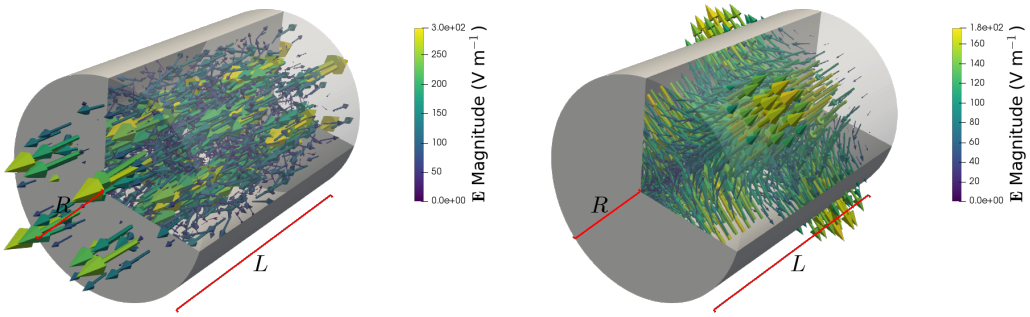

Figure 7: Representation of a pillbox cavity of radius $R = 35\,\text{mm}$ and length $L = 100\,\text{mm}$ with the electric field $\boldsymbol{E}$ associated to the eigenfunction $TM423$ (left) and $TE212$ (right).

are given by

$$\omega^{TM}_{mnq} = \frac{1}{\sqrt{\epsilon\mu}}\sqrt{\frac{\chi^2_{mn}}{R^2} + \frac{q^2\pi^2}{L^2}}\ , \qquad \omega^{TE}_{mnq} = \frac{1}{\sqrt{\epsilon\mu}}\sqrt{\frac{\chi'^2_{mn}}{R^2} + \frac{q^2\pi^2}{L^2}}\ ,$$

where χ_{mn} and χ'_{mn} are the n-th root of the Bessel function of the first kind of order m and of its derivative, respectively. The value m is the Fourier mode of the

corresponding eigenfunction. As a consequence, for each m we can compute the eigenvalues varying the values of q and n. In the following we consider the case $\omega \neq 0$.

Using cylindrical coordinates and applying the method presented in this work, we end up with a set of independent two-dimensional problems for each mode $m \neq 0$ whose weak formulation is given by (9). After the discretization step we have to find the eigenpairs $(\lambda^2_{i,\,m},\, \mathbf{v}_{i,\,m})$ of linear system

$$\mathbf{A}_m \mathbf{v}_{i,\,m} = \lambda^2_{i,\,m} \mathbf{M}_m \mathbf{v}_{i,\,m} \ ,$$

where $\mathbf{A}$ is associated to the discretization on the curl-curl operator, $\mathbf{M}$ is the mass matrix and $\lambda_{i,\,m}$ is an approximation of ω_{mnq} for a specific value of nq.

In Figure 8, the exact value of the first 10 angular frequencies for $m = 26$ are represented by horizontal blue lines. In the same figure, the approximated angular frequencies are shown for different values of subdivisions of the parametric section (h-refinement) and using a uniform discretization and a maximum degree $p = 3$. It can be seen that no spurious modes appear and that the computed

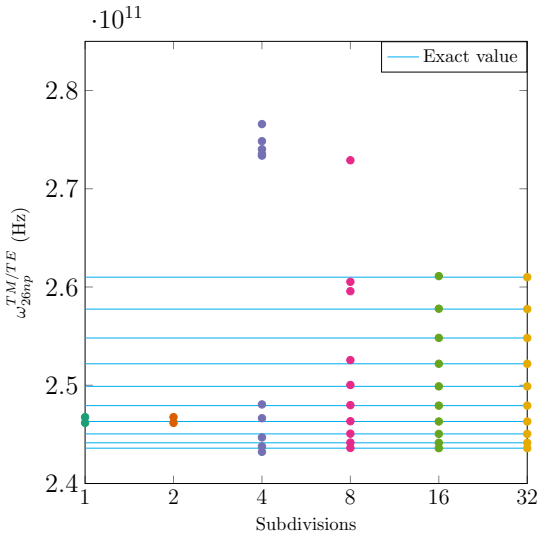

Figure 8: Approximations of the first 10 angular frequencies ($m = 26$) for different number of subdivision of the parametric section. The exact values are represented by horizontal blue lines.

eigenvalues converge to the exact ones. To test the approximation properties of our discretization, a specific eigenvalue ω^{TE}_{134} has been chosen and the error for different subdivisions and degrees p has been computed. In Figure 9, the error trends with respect to the to h-refinement (left) and to the number of DoFs (right) are shown. It can be seen that the approximate eigenvalues converges with a rate equal to the double of the polynomial degree p employed in the discretization, which corresponds to the behaviour predicted by the theory [22].

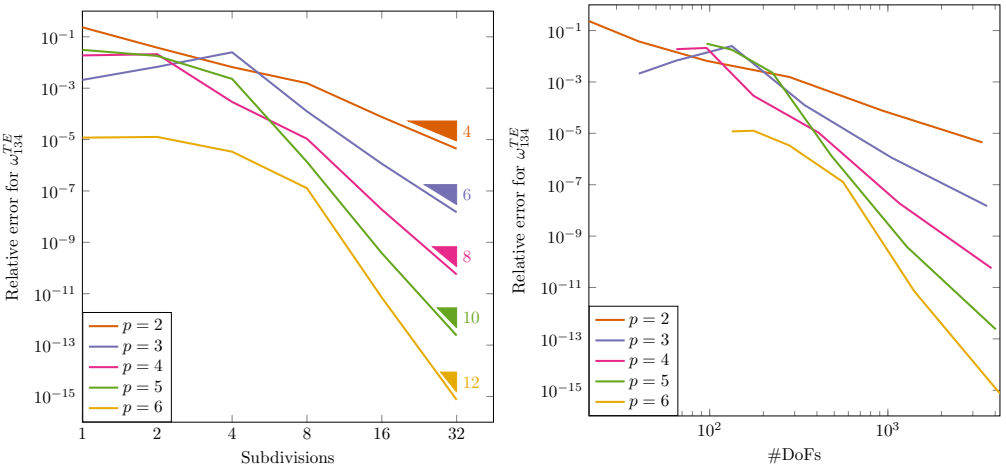

Figure 9: Relative error with respect to the number of subdivision of the parametric cross-section $\widehat{S}$ (left) and with respect to the number of DoFs (right) for the angular frequency ω_{134}^{TE}.

5.3 TESLA cavity

In this section, we solve again the eigenvalue problem (36), but on a domain which has a higher practical relevance and whose geometry is defined using a NURBS surface. The specific design used in this test is the one-cell midcup TESLA cavity whose precise definition can be found in [23, Table III]. We consider the problem of approximating the lowest resonant angular frequency for the modes $m = 1$ and $m = 2$ which are, respectively,

$$\omega_1 \approx 11\,468.32\,\text{MHz} \quad \text{and} \quad \omega_2 = 14\,582.56\,\text{MHz}\ .$$

In Figure 10, the eigenfunctions associated to the considered eigenvalues are depicted. In Figure 11, the trend of the relative errors, estimated as the relative difference between two subsequent refinement levels, are shown. Also in this case, it can be seen that the approximate eigenvalues converge with a rate close to twice the polynomial degree p employed in the discretization.

6 Conclusions and future perspectives

In the context of electromagnetic problems on axisymmetric domains, we have presented and analysed a combination of a spectral Fourier approximation in the azimuthal direction with an IsoGeometric Analysis (IGA) approach in the radial and axial directions. The resulting method provides discrete approximations that, thanks to an appropriate choice of the finite-dimensional approximation spaces, preserves, at the discrete level, the structure of the continuous Maxwell equations. Rigorous error estimates have been obtained for the proposed method, along with

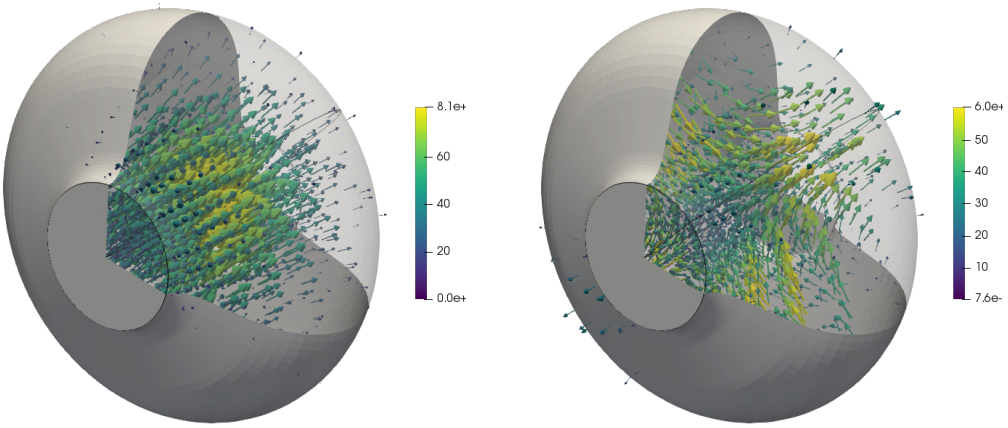

Figure 10: TESLA cavity. Eigenfunctions associated to the lowest eigenvalues for the modes $m = 1$ (left) and $m = 2$ (right).

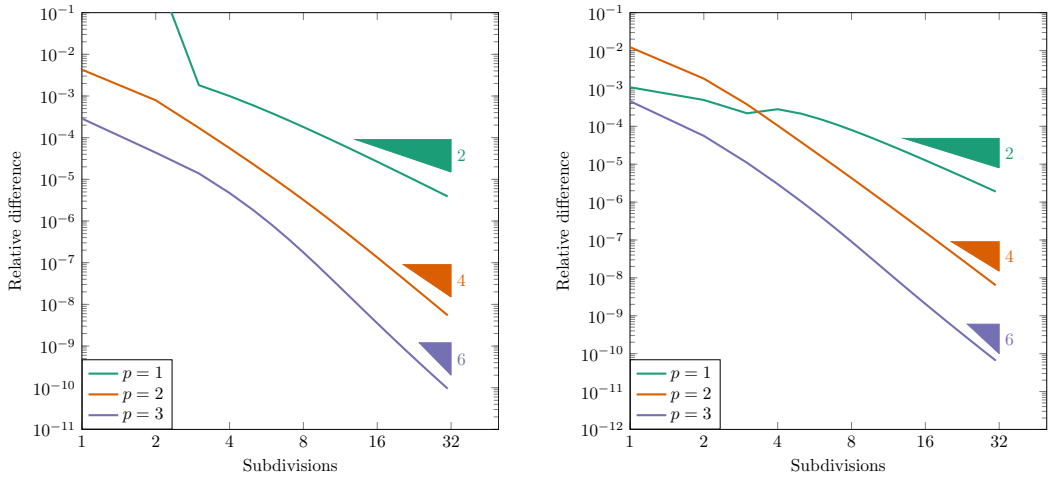

Figure 11: TESLA cavity. Error on the lowest eigenvalues $m = 1$ (left) and $m = 2$ (right) with respect to the number of subdivisions for different degrees p of the basis functions.

the proof that the associated discrete functional spaces form a de Rham complex that is closed and exact. A number of numerical benchmarks have been considered, yielding also empirical evidence that the resulting method combines the capability of the IGA approach to represent very accurately complex geometries, achieves high convergence rates and allows to decouple the computation associated to different Fourier modes.

In future developments, it is planned to apply the proposed approach to the

reconstruction of magnetic fields to be used for the simulation of particle accelerators, in order to complement the results obtained in [10] with high order particle tracking methods with an equally accurate and physically sound representation of the magnetostatic fields involved in these simulations.

Acknowledgements

This paper contains some of the results obtained by the first author in his PhD thesis work, which has been supervised jointly by the other authors. This work has been carried out in the framework of a joint PhD agreement between Politecnico di Milano and Technische Universität Darmstadt. It has been partially supported by the 'Excellence Initiative' of the German Federal and State Governments and the Graduate School of Computational Engineering at Technische Universität Darmstadt. We would like to thank Kersten Schmidt for the fruitful discussions and Minah Oh for several explanations concerning the properties of exact sequences of finite-dimensional spaces presented in her papers.

References

[1] F. Assous, P. Ciarlet Jr, S. Labrunie, Theoretical tools to solve the axisymmetric Maxwell equations, Mathematical Methods for the Applied Sciences 25 (2002) 49–78.

[2] C. Bernardi, M. Dauge, Y. Maday, M. Azaïez, Spectral methods for axisymmetric domains, Vol. 3, Gauthier-Villars Paris, 1999.

[3] S. Börm, R. Hiptmair, Multigrid computation of axisymmetric electromagnetic fields, Advances in Computational Mathematics 16 (2002) 331–356.

[4] D. M. Copeland, J. E. Pasciak, A least-squares method for axisymmetric div–curl systems, Numerical Linear Algebra with Applications 13 (2006) 733–752.

[5] D. Copeland, J. Gopalakrishnan, M. Oh, Multigrid in a weighted space arising from axisymmetric electromagnetics, Mathematics of Computation 79 (2010) 2033–2058.

[6] J. Gopalakrishnan, M. Oh, Commuting smoothed projectors in weighted norms with an application to axisymmetric Maxwell equations, Journal of Scientific Computing 51 (2012) 394–420.

[7] H. Li, Finite element analysis for the axisymmetric Laplace operator on polygonal domains, Journal of computational and applied mathematics 235 (2011) 5155–5176.

[8] B. Mercier, G. Raugel, Résolution d'un problème aux limites dans un ouvert axisymétrique par éléments finis en r, z et séries de Fourier en θ, RAIRO. Analyse numérique 16 (4) (1982) 405–461.

[9] M. Oh, de Rham complexes arising from Fourier finite element methods in axisymmetric domains, Computers & Mathematics with Applications 70 (8) (2015) 2063–2073.

[10] A. Simona, L. Bonaventura, T. Pugnat, B. Dalena, High order time integrators for the simulation of charged particle motion in magnetic quadrupoles., Computer Physics Communications 239 (2019) 33–52.

[11] S. Perotto, A. Reali, P. Rusconi, A. Veneziani, HIGAMod: A hierarchical isogeometric approach for model reduction in curved pipes, Computers & Fluids 142 (2017) 21–29.

[12] Z. Bontinck, J. Corno, H. De Gersem, S. Kurz, A. Pels, S. Schöps, F. Wolf, C. de Falco, J. Dölz, R. Vázquez, U. Römer, Recent advances of isogeometric analysis in computational electromagnetics, ICS Newsletter (International Compumag Society) 3. arXiv:1709.06004.
URL `http://www.compumag.org/jsite/images/stories/newsletter`

[13] A. Buffa, G. Sangalli, R. Vázquez, Isogeometric analysis in electromagnetics: B-splines approximation, Computer Methods in Applied Mechanics and Engineering 199 (2010) 1143–1152.

[14] P. Monk, et al., Finite element methods for Maxwell's equations, Oxford University Press, 2003.

[15] J. Corno, C. de Falco, H. De Gersem, S. Schöps, Isogeometric simulation of Lorentz detuning in superconducting accelerator cavities, Computer Physics Communications 201 (2016) 1–7.

[16] C. Arioli, A. Shamanskiy, S. Klinkel, B. Simeon, Scaled boundary parametrizations in isogeometric analysis, Computer Methods in Applied Mechanics and Engineering 349 (2019) 576–594.

[17] J. D. Jackson, Classical electrodynamics, John Wiley & Sons, 2007.

[18] A. Buffa, J. Rivas, G. Sangalli, R. Vázquez, Isogeometric discrete differential forms in three dimensions, SIAM Journal on Numerical Analysis 49 (2) (2011) 818–844.

[19] A. Buffa, G. Sangalli, R. Vázquez, Isogeometric methods for computational electromagnetics: B-spline and T-spline discretizations, Journal of Computational Physics 257 (2013) 1291–1320.

[20] I. Higueras, T. Roldán, J. J. Torrens, Numerical Simulation in Physics and Engineering, Springer, 2016.

[21] D. Boffi, Finite element approximation of eigenvalue problems, Acta Numerica 19 (2010) 1–120.

[22] D. N. Arnold, R. Falk, R. Winther, Finite element exterior calculus: from hodge theory to numerical stability, Bulletin of the American mathematical society 47 (2) (2010) 281–354.

[23] B. Aune, R. Bandelmann, D. Bloess, B. Bonin, A. Bosotti, M. Champion, C. Crawford, G. Deppe, B. Dwersteg, D. Edwards, et al., Superconducting TESLA cavities, Physical Review Special Topics-Accelerators and Beams 3 (9) (2000) 092001.

MOX Technical Reports, last issues

Dipartimento di Matematica
Politecnico di Milano, Via Bonardi 9 - 20133 Milano (Italy)

53/2019 Cerroni, D., Penati, M.; Porta, G.; Miglio, E.; Zunino, P.; Ruffo, P.
Multiscale modeling of glacial loading by a 3D Thermo-Hydro-Mechanical approach including erosion and isostasy

52/2019 Cerroni, D.; Radu, A. R. ; Zunino, P.
Numerical solvers for a poromechanic problem with a moving boundary

51/2019 Parolini, N.; Riccobene, C.; Schenone, E.
Reduced models for liquid food packaging systems

49/2019 Cicchetti, A.; Laurino, F.; Possenti, L.; Rancati, T.; Zunino, P.
In silico model of the early effects of radiation therapy on the microcirculation and the surrounding tissues

50/2019 Lusi, V.; Moore, T. L.; Laurino, F.; Coclite, A.; Perreira, R.; Rizzuti, I.; Palomba, R.; Zunino, P
A tissue chamber chip for assessing nanoparticle mobility in the extravascular space

48/2019 Di Gregorio, S.; Fedele, M.; Pontone, G.; Corno, A.F.; Zunino, P.; Vergara, C.; Quarteroni, A.
A multiscale computational model of myocardial perfusion in the human heart

47/2019 Spreafico, M.; Ieva, F.
Dynamic monitoring of the effects of adherence to medication on survival in Heart Failure patients: a joint modelling approach exploiting time-varying covariates

46/2019 Di Iorio, J.; Vantini, S.
funBI: a Biclustering Algorithm for Functional Data

44/2019 Formaggia, L.; Gatti, F.; Zonca, S.
An XFEM/DG approach for fluid-structure interaction problems with contact

45/2019 Regazzoni, F.; Dedè, L.; Quarteroni, A.
Active force generation in cardiac muscle cells: mathematical modeling and numerical simulation of the actin-myosin interaction